ANALYTICAL METHODS DEVELOPMENT FOR HIGH-THROUGHPUT PHOTOCHEMISTY WITH LED ARRAYS

By

Jared R. Brown

Thesis submitted to the faculty of the Virginia Polytechnic Institute and State University
in partial fulfillment of the requirements for the degree of

Master of Science

In

Chemistry

Karen J. Brewer, Chair
Mark Anderson, Member
Gordon T. Yee, Member
J. M. Tanko, Member
Paul Deck, Member

May 3, 2007

Blacksburg, Virginia

Keywords: LED, Actinometry, Photochemistry, High-Throughput, and Pedestrians.

ANALYTICAL METHODS DEVELOPMENT FOR HIGH-THROUGHPUT PHOTOCHEMISTY WITH LED ARRAYS

Jared R. Brown

(ABSTRACT)

This thesis describes the design, construction, and evaluation of a series of LED array photolysis systems for high throughput photochemistry. Three generations of array systems of increasing sophistication are evaluated using calorimetric measurements and potassium tris(oxalato)ferrate(III) chemical actinometry. The results are analyzed using descriptive statistics and analysis of variance (ANOVA). The LEDs in the third generation array were shown to be statistically equivalent, with respect to light output, according to physical and chemical actinometry experiments. The third generation LED array was compared with a traditional 1000 W Xe arc lamp source in terms of cost, light intensity, and light stability. Two constant current drivers were evaluated with respect to LED array performance. The optimized third generation LED array was evaluated as the photolysis source for photochemical hydrogen production experiments using the supramolecular catalyst $[\{(bpy)_2Ru(dpp)\}_2RhCl_2](PF_6)_5$.

To my wonderful wife Lorrie, my daughters Abigail and Sarah, and all of my family

ACKNOWLEDGMENTS

This academic accomplishment could not have been possible without the help and support of many people. I am deeply grateful to all of them:

to my research advisor, Dr. Karen J. Brewer, for your patience, guidance, and support in the completion of this research;

to the members of my graduate committee: Dr. Gordon Yee, Dr. Paul Deck, Dr. James Tanko, and Dr. Mark Anderson for your helpful suggestions and insight;

to Thomas Wertalik for you construction of the LED photolysis cells, and other glass shop needs;

to Melvin and the guys from the physics machine shop for the materials and training;

to John Burleson for the discussions on electronics

to my fellow graduate students: David Zigler, Mark Elvington, Avijita Jain, Joan Zapiter, Ran Miao, Shangliang Zhao for all the support and laughter;

to Drs. Matthew Mongelli and Shamindri Arachchige for your help and friendship;

to Dr. Gary Long for the discussions about statistics and analysis of variance;

to my grandfather William E. Brown for discussions on electronics and shoptalk;

to my parents William E. Brown Jr. and Jennifer Brown for the love, support, and babysitting that made this all possible;

and to my wife Lorrie and my daughters Abigail and Sarah you are why I am here I love you.

TABLE OF CONTENTS

LIST OF FIGURES

LIST OF TABLES

LIST OF ABBREVIATIONS

LCAO	Linear Combination of Atomic Orbitals
MO	Molecular Orbital
HOMO	Highest Occupied Molecular Orbital
LUMO	Lowest Unoccupied Molecular Orbital
IL	Intra-Ligand
LF	Ligand Field
MLCT	Metal-to-Ligand Charge Transfer
LMCT	Ligand-to-Metal Charge Transfer
LA	Light Absorber
LA*	Light Absorbing Species in the Excited State
ED	Electron Donor
CAT	Catalyst
dpb	2,3-bis(2-pyridyl)benzoquinoxaline
dpp	2,3-bis(2-pyridyl)pyrazine
phen	1,10-phenanthroline
bpy	2,2'-bipyridine
TEOA	Triethanolamine
Me_6[14]4,11-dieneN_4	5,7,7,12,14,14-hexamethyl-1,4,8,11-tetraazacyclotetradeca-4,11-diene

dmphen	4,4’-diphenylphenanthroline
tatpp	9,11,20,22-tetraazatetrapyrido[3,2-a:2’3’-c:3”,2”-/:2’’’,3’’’]pentacene)
dfpma	bis(difluorophosphino)methylamine
LED	Light Emitting Diode
ANOVA	Analysis of Variance
FWHM	Full Width at Half Maximum
spdt	Single Pole Double Throw

Chapter 1. INTRODUCTION

1.1 Research Goals

Our goals were to design, construct, and evaluate a series of LED array photolysis systems for high throughput photochemistry. The LED arrays were compared with a traditional 1000 W Xe arc lamp source in terms of cost, light intensity, and light stability. Constant current drivers were evaluated with respect to LED array performance. The optimized third generation LED array was evaluated as the photolysis source for photochemical hydrogen production experiments using the supramolecular catalyst $[\{(bpy)_2Ru(dpp)\}_2RhCl_2](PF_6)_5$. All results were analyzed using descriptive statistics and analysis of variance (ANOVA).

1.2 Review of Related Literature

1.2.1 Solar Energy Conversion

The need for renewable energy has driven research for more than thirty years. Developing the technology to use renewable resources is especially important today with diminishing oil reserves and unstable world politics. One major source of renewable energy is solar energy. Figure 1.1 shows a solar irradiance spectrum at the Earth's surface highlighting the energy density of sunlight.[1] It has been reported that the annual solar energy received by the Earth is 5.0×10^{21} kJ.

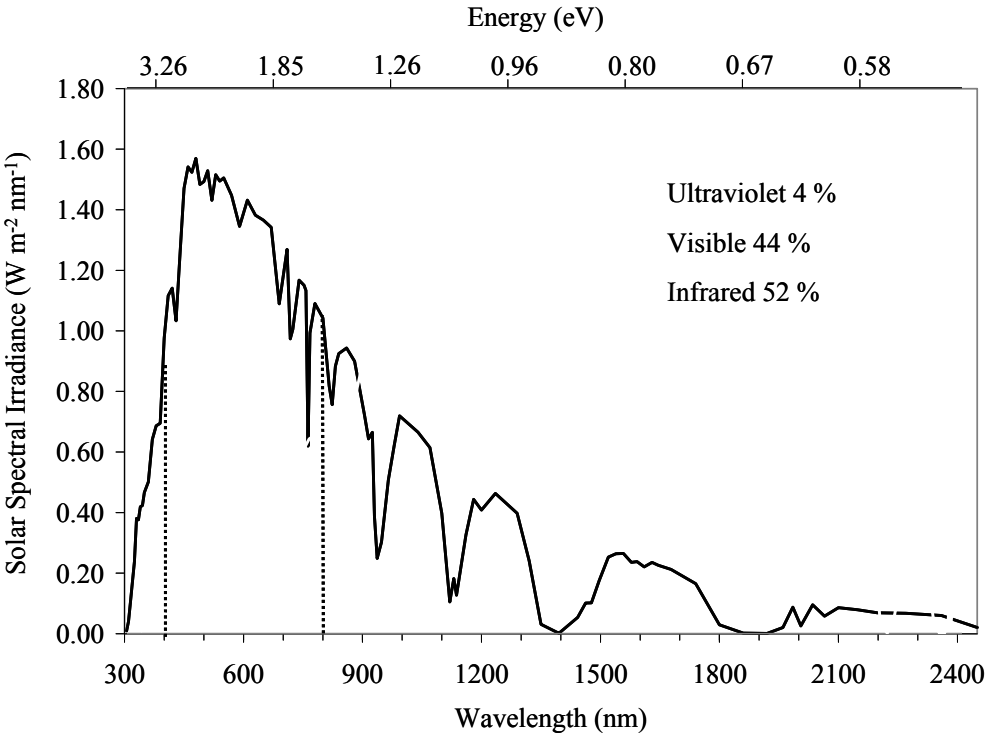

Figure 1.1 Solar spectral irradiance spectrum at the earth's surface with the energy density of the spectrum highlighted.[1]

Much of the energy received is reflected (33 %), however, 7.5×10^{20} kJ is absorbed by the world's continents.[2] The total world's marketed energy consumption in 2003 was 4.4×10^{17} kJ, which constitutes 0.06 % of the energy that is absorbed by the land.[3]

1.2.2 Solar Water Splitting

Currently plants convert solar energy through photosynthesis. This energy is passed on to animals by way of consumption, or is converted to oil. A faster approach to solar energy conversion is required. Investigators have probed methods of direct solar energy conversion since the early seventies.[4,5] Solar energy has been utilized in light to

energy conversion schemes through several mechanisms including thermal processes such as solar concentrators, photobiological processes, photoelectrical processes such as solar cells, and photochemical processes such as solar water splitting. In solar water splitting, the mechanism for solar energy conversion is through the production of an energy feedstock, hydrogen and oxygen. Thus, the decomposition of water to hydrogen and oxygen has been the subject of much research. Table 1.1 lists several half reactions important to solar hydrogen production.[2]

Balzani addressed the problems with transition metal systems for solar water splitting.[4] Transition metal systems which attempted solar water splitting through a one electron process reported very meager results. This is due to the energy cost of forming H· as an intermediate step to H_2, and therefore these systems can only function in the UV. Equation 1.1 lists the most energetically feasible water splitting reaction from those listed in table 1.1.

$$H_2O \rightarrow \frac{1}{2} O_2 + H_2 \text{ (237.2 kJ, 1.23 eV)} \qquad (1.1)$$

Water splitting at an energetically feasible driving force is a multi-electron process, and it requires a multi-electron solution.

Table 1.1 Thermodynamic data for some reactions involving water and its fragments.[2]

Reaction	$\Delta G°_{298}$ (kJ)	E°, V (vs. NHE)
$H_2O \rightarrow \frac{1}{2} O_2 + 2 H^+ + 2 e^-$	237.2	1.23
$H_2O \rightarrow O· + 2 H^+ + 2 e^-$	467.4	2.421
$OH^- + \frac{1}{2} H_2 \rightarrow H_2O + 2 e^-$	-79.9	-0.828
$H_2 \rightarrow 2 H^+ + 2 e^-$	0	0
$H· \rightarrow H^+ + e^-$	-203.4	-2.11

1.2.3 Molecular Orbital Description of an Octahedral Complex

In order to understand the functioning of the components in a photochemical water splitting system, it is first important to understand a molecular orbital description of the metal complexes. The d^6 pseudo octahedral metal complexes can be described according to a linear combination of atomic orbitals (LCAO), Figure 1.2A. In this picture each block molecular orbital is composed of a combination of molecular orbitals. The shaded orbital sets are occupied, and the unshaded orbital sets are vacant. The d^6 complexes often are often characterized by having metal based highest occupied molecular orbital, HOMO, and ligand based lowest unoccupied molecular orbital, LUMO. Upon absorption of light, electronic transitions may occur such that an electron is promoted from an occupied orbital to an unoccupied orbital. These electronic transitions are designated by the orbitals involved, Figure 1.2B.[6] Transitions localized on ligand orbitals are termed intra-ligand, IL. Transitions localized on the metal orbitals are termed ligand field transitions, LF. Transitions involving ligand and metal orbitals are either ligand to metal charge transfers, LMCT, or metal to ligand charge transfers, MLCT. The transition of an electron from a filled orbital to an unfilled orbital results in a new molecular orbital configuration. This new configuration is termed a state.

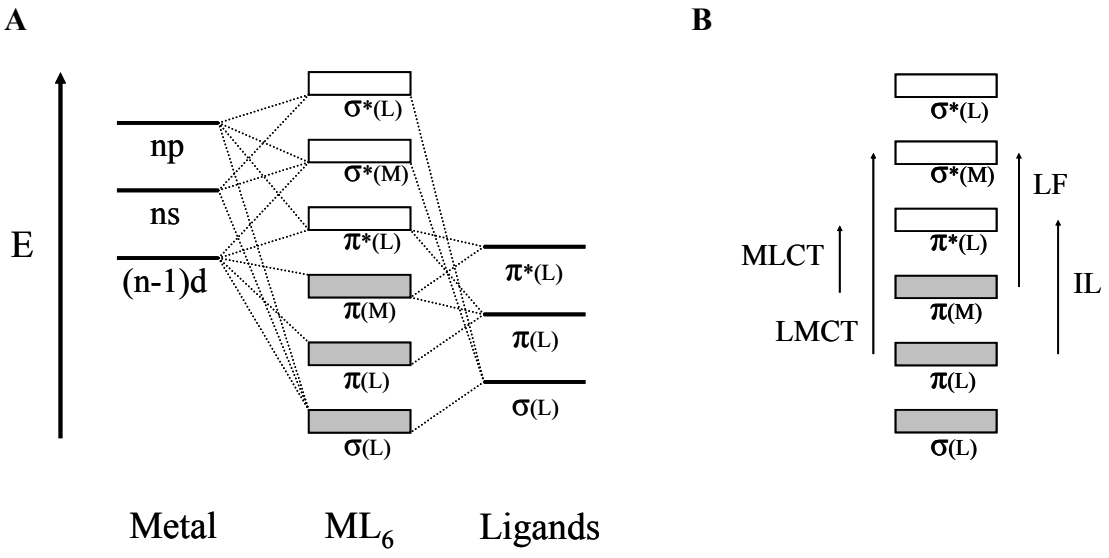

Figure 1.2 A. Block molecular orbital diagram for an octahedral complex. The shaded blocks represent occupied orbitals. **B.** Block orbital diagram showing possible electronic transitions common in an octahedral complex.[6]

1.2.4 Components of a Water Splitting System

Several approaches exist for photochemical hydrogen production. Of note are heterogeneous systems based on semiconductors, heterogeneous multi-molecular systems which utilize colloidal metals as microelectrodes, homogenous multi-molecular systems, and homogeneous supramolecular systems.[7-9] The present work, which is focused on improved light sources for use in photochemical hydrogen production, is limited in scope to homogeneous molecular systems for photochemical hydrogen production. Balzani points out that there are three basic components of a photochemical system for water splitting based on transition metal catalysts:[4,7] (1) Visible light absorption, (2) conversion of the excitation energy to redox energy, and (3) concerted transfer of multiple electrons

to water. These components are made use of in multi-molecular systems and supramolecular assemblies.

1.2.5 Light Absorbing Unit

An essential part of a solar energy conversion scheme is the light absorbing unit (LA). The electronic absorption spectrum of the light absorbing unit must overlap the emission spectrum of the sun to the greatest extent possible. Upon absorption of light the LA must undergo electronic excitation. Typical LAs used in multi-molecular and supramolecular solar energy conversion schemes are ruthenium and osmium polyazine complexes. Typical polyazine ligands used in ruthenium and osmium light absorbing complexes are shown in Figure 1.3. Ruthenium and osmium polyazine complexes are known to absorb light efficiently throughout the UV and visible regions. The prototypical chromophore, $[Ru(bpy)_3]^{2+}$ is characterized by intense ligand based $\pi \rightarrow \pi^*$ and $n \rightarrow \pi^*$ transition in the UV region and a strong metal-to-ligand charge transfer, MLCT, in the visible region

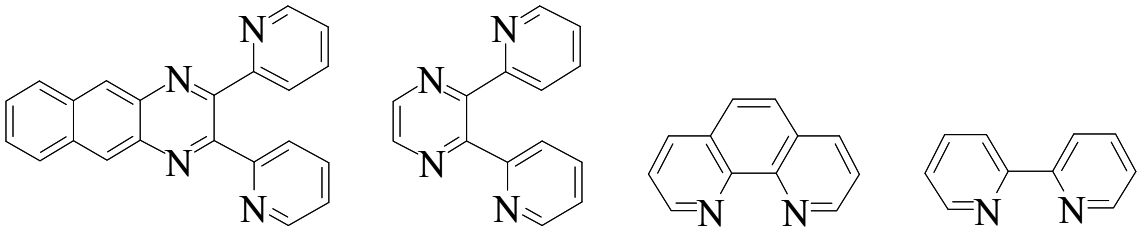

Figure 1.3 A series of polyazine ligands typically used in ruthenium and osmium light absorbing complexes (dpb = 2,3-bis(2-pyridyl)benzoquinoxaline, dpp = 2,3-bis(2-pyridyl)pyrazine, phen = 1,10-phenanthroline, and bpy = 2,2'-bipyridine).

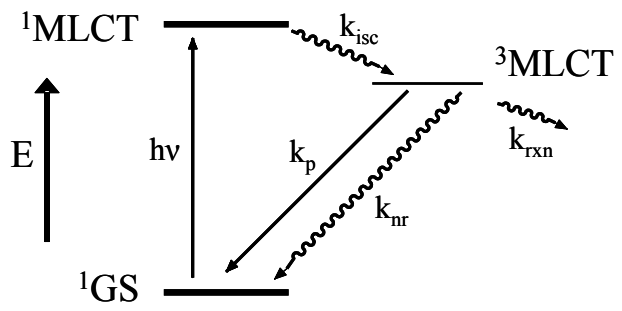

Figure 1.4 State diagram for $[Ru(bpy)_3]^{2+}$ showing optical population of the singlet metal-to-ligand charge transfer (^{1}MLCT) state and intersystem crossing to the ^{3}MLCT state (bpy = 2,2'-bipyridine).

(bpy = 2,2'-bipyridine). The MLCT transition is characterized by the movement of an electron from the metal based dπ orbital to the ligand based π* orbital, which can be thought of as a metal oxidation and a ligand reduction. The transition to the MLCT state makes the complex a better oxidizing and reducing agent relative to the ground state. Figure 1.4 is a state diagram showing the excited state processes for $[Ru(bpy)_3]^{2+}$. Upon excitation the ^{1}MLCT is populated. The ^{1}MLCT rapidly decays through an intersystem crossing (isc) into the ^{3}MLCT state with unit efficiency. The ^{3}MLCT state of ruthenium polyazine complexes is typically long-lived (τ = 600 ns at 25 °C for $[Ru(bpy)_3]^{2+}$). The ^{3}MLCT is depopulated by radiative decay (r), nonradiative decay (nr), or by energy or electron transfer (rxn).

1.2.6 Conversion of Excitation Energy to Redox Energy

The ^{3}MLCT excited state of ruthenium polyazine complexes is able to undergo reductive and oxidative excited state electron transfer reactions. Electron transfer is essential to

photoinitiated hydrogen production. Figure 1.5A is a generalized schematic of photoinitiated hydrogen production by a reductive quenching mechanism. The ^{3}MLCT is reductively quenched by the electron donor, ED. The resulting species LA^- is a stronger reducing agent than LA*, allowing for redox reaction with the catalyst, resulting in hydrogen production. Figure 1.5B represents the generalized oxidatively quenched pathway for a O_2 production, where EA is the electron acceptor which oxidatively quenches the light absorber LA to LA^+.[7] The reductive and oxidative excited state electron transfer reactions can be utilized in an intramolecular sense in supramolecular assemblies built using Ru and Os type LA units. In a four component microheterogenous system composed of $[Ru(bpy)_3]^{2+}$ LA, $[Rh(bpy)_3]^{2+}$ electron relay, triethanolamine (TEOA) as ED, and a colloidal Pt catalyst, the Rh functions as an electron acceptor and relay in the intermolecular electron transfer from the LA to the CAT. Tris(polyazine)rhodium(III) complexes are known to serve as electron acceptors in

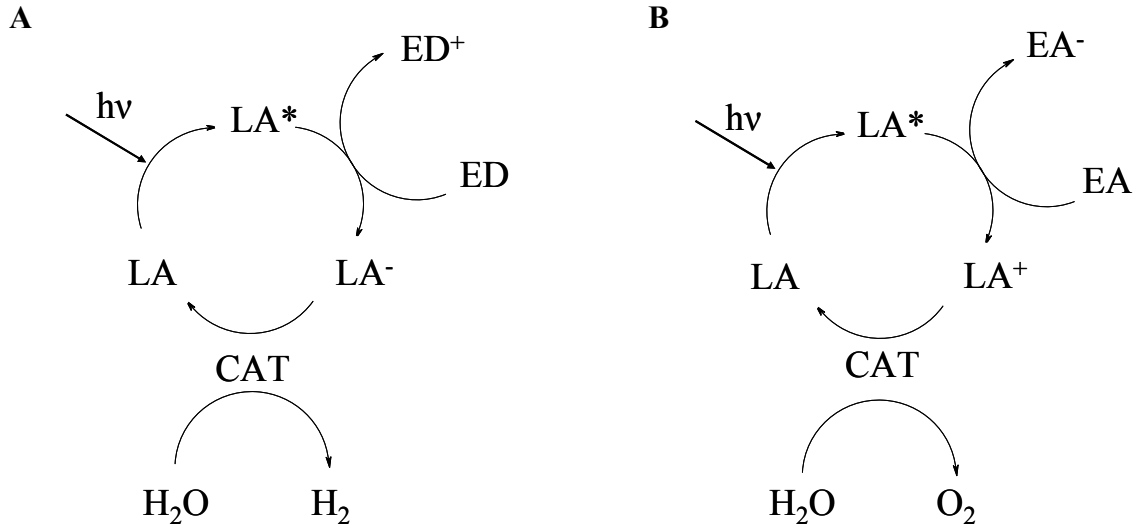

Figure 1.5 Schematics of photochemical hydrogen production by **A.** a reductively quenching mechanism and **B.** an oxidatively quenching mechanim.[7]

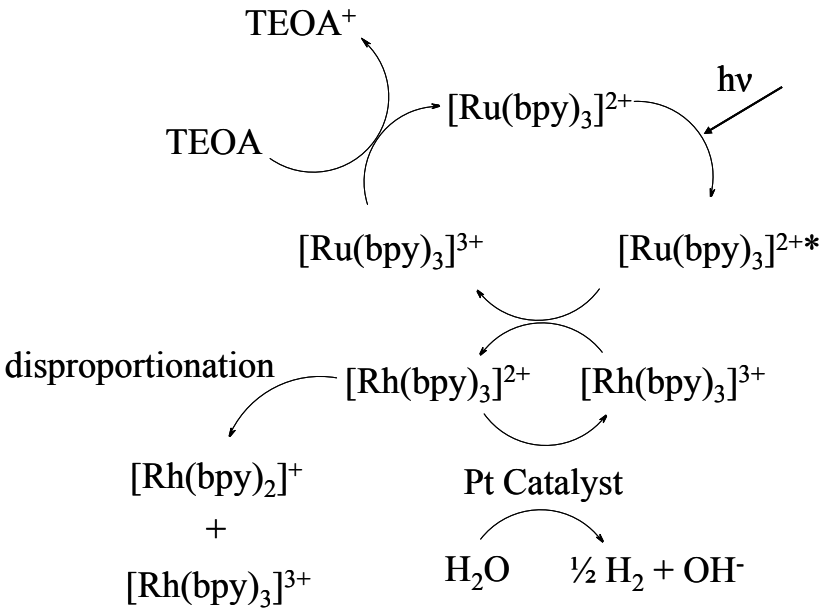

Figure 1.6 Schematic of photochemical hydrogen production using a four component system with $[Ru(bpy)_3]^{2+}$ as the light absorber, $[Rh(bpy)_3]^{3+}$ the electron relay, triethanolamine (TEOA) the electron donor, and colloidal platinum was used as a catalyst. In the absence of Pt, $[Rh(bpy)_3]^{2+}$ will disproportionate to $[Rh(bpy)_3]^{3+}$ and $[Rh(bpy)_3]^{2+}$ (bpy = 2,2'-bipyridine).[10,11]

intermolecular electron transfer schemes utilizing $[Ru(bpy)_3]^{2+}$ light absorbers, resulting in the transfer of electrons into a Rh(dσ*) acceptor orbital. The newly generated Rh^{II} state is subject to disproportionation to $[Rh(bpy)_2]^{+}$ and $[Rh(bpy)_3]^{3+}$ in the absence of the colloidal platinum catalyst, Figure 1.6.[11,12]

1.2.7 Homogeneous Catalysts in Multi-Molecular Systems

Water splitting at a lower driving force requires multi-electron chemistry. Homogenous transition metal catalysts must be able to access a variety of oxidation states for concerted multi-electron transfer. There are no homogenous systems capable of photocatalytically generating hydrogen and oxygen from water. The discussion will,

therefore, be limited to the few homogeneous photochemical catalysts for hydrogen production. Presently, the only homogeneous transition metal systems for hydrogen production utilize Rh or Co catalysts, with Co being the most studied. Cobalt systems have been shown to follow homosynthetic and heterosynthetic mechanisms. One of the main advantages of homogenous catalysis is the ability to modulate the nature of the individual components of the system: LA, ED, CAT. In a system composed of $[Ru(bpy)_3]^{2+}$ (LA) and ascorbate (pH 5) (ED) there was a 100 fold increase in the rate of hydrogen evolution on changing from the macrocyclic complex, $[Co(Me_6[14]4,11\text{-}dieneN_4)]^{2+}$, to the polyazine complex, $[Co(bpy)_3]^{2+}$ ($Me_6[14]4,11\text{-}dieneN_4$ = 5,7,7,12,14,14-hexamethyl-1,4,8,11-tetraazacyclotetradeca-4,11-diene, Figure 1.7B).

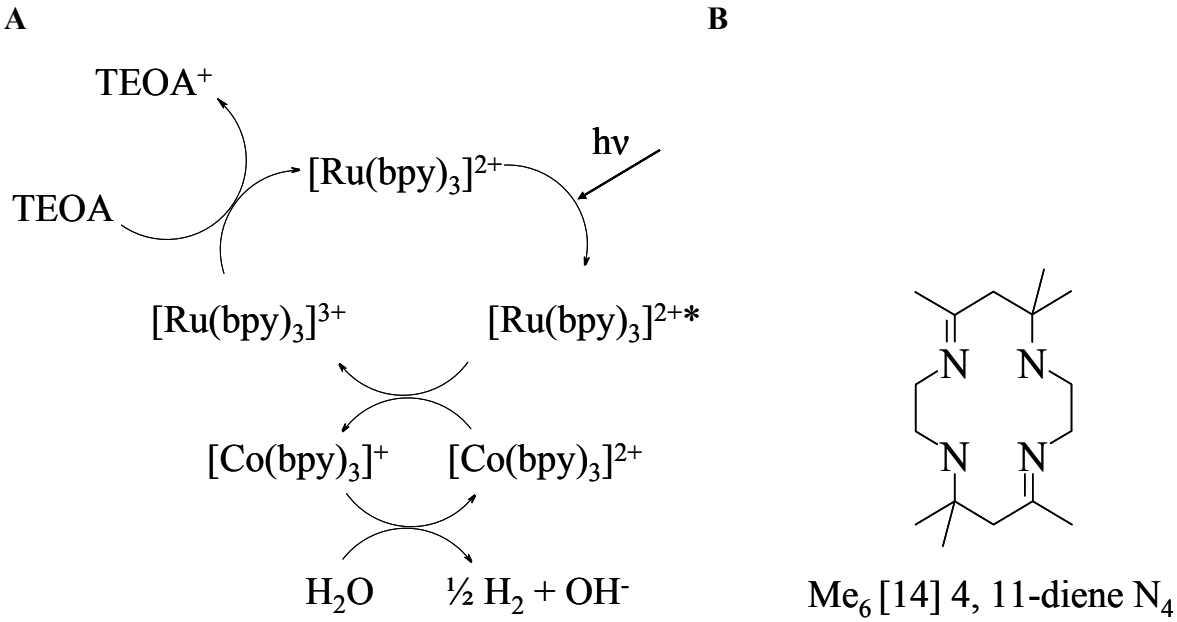

Figure 1.7 A. Schematic of photochemical hydrogen production using a three component system with $[Ru(bpy)_3]^{2+}$ as the light absorber, $[Co(bpy)_3]^{2+}$ the electron relay / homogeneous catalyst, and triethanolamine (TEOA) as the electron donor. **B.** macrocyclic ligand (Me_6 [14] 4,11-diene N_4 = 5,7,7,12,14,14-hexamethyl-1,4,8,11-tetraazacyclotetradeca-4,11-diene, bpy = 2,2'-bipyridine))[13]

Several trends have been observed. On increasing the concentration of triethanolamine (ED) in a $[Ru(bpy)_3]^{2+}$, $[Co(bpy)_3]^{2+}$ system, Figure 1.7A, Creutz observed a ten-fold increase in the rate of hydrogen evolution with a five-fold increase in ED.[13] As many systems are aqueous, optimizing pH is key, and often the optimum pH was found to be equal to the pKa of the ED. The concentrations of the LA and CAT also impact the system functioning. It has been observed that an increase in CAT improves system function initially, followed by a leveling off, Figure 1.8A. This is postulated to be a shutdown due to CAT – CAT interaction. Upon increasing the concentration of the LA Bernhard observed that system

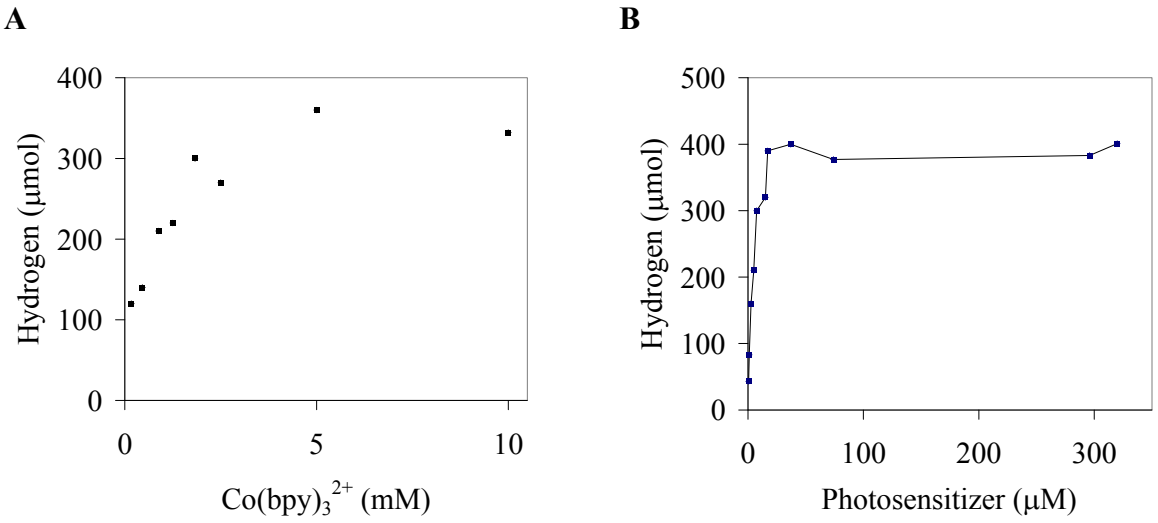

Figure 1.8 A. Hydrogen evolution vs. concentration of $[Co(bpy)_3]^{2+}$. All experiments contained 300 μM $[Ru(dmphen)_3]^{2+}$ (the photosensitizer), cobalt catalyst, 0.57 M triethanolamine (TEOA), and 0.27 M LiCl in 50:50 water/acetonitrile. The pH was adjusted by the addition of 0.4 mL of 12 M HCl (total solution volume was 20 mL. **B.** Hydrogen evolution vs. the concentration of the photosensitizer $[Ru(dmphen)_3]^{2+}$ (dmphen = 4,4'-diphenylphenanthroline). All experiments contained the photosensitizer, 2.5 mM $[Co(bpy)_3]^{2+}$, 0.57 M triethanolamine (TEOA), and 0.27 M LiCl in 50:50 water/acetonitrile. The pH was adjusted by the addition of 0.4 mL of 12 M HCl (total solution volume was 20 mL. The solid line is a guide for the eye.

functioning increased dramatically, then leveled off. This was attributed to complete absorbance of light, Figure 1.8B

1.2.8 Supramolecular Device for Electron Collection

A 1987 landmark monograph by Balzani proposed the use of supramolecular species for complex functions. A supramolecule can be thought of as a large unit composed of smaller units, all which are able to contribute functionality to the whole. One such application is photoinitiated electron collection. Multi-electron chemistry is essential to small molecule activation such as solar hydrogen production. Despite the importance of photoinitiated electron collection in small molecule activation only a few functioning photoinitiated electron collectors exist. This is due in part to the lack of understanding of the factors which impact multi-electron photochemistry as well as the complexity of the photoinitiated electron collection process. The first functioning photoinitiated electron collector was reported by Brewer.[14] The system was composed of two Ru LAs connected through bridging ligands, BL, to an Ir core. $[\{(bpy)_2Ru(dpb)\}_2IrCl_2](PF_6)_5$ collected electrons onto the π conjugated bridging ligands (dpb = 2,3-bis(2-pyridyl)benzoquinoxaline). Due to their separation by the Ir centers the two ruthenium LAs are electronically isolated, and each are capable of MLCT to the bridging ligands.

MacDonnell and Campagna reported two interesting Ru-Ru bimetallic complexes that photochemically collect either two or four electrons. These systems

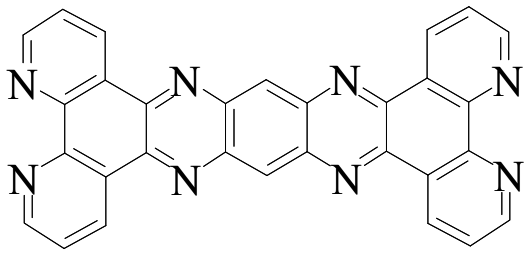

tatpp

Figure 1.9 The orbital structure of tatpp allows for collection of up to four electrons in the complex $[(phen)_2Ru(tatpp)Ru(phen)_2]^{4+}$ (tatpp = 9,11,20,22-tetraazatetrapyrido[3,2-a:2'3'-c:3",2"-/:2''',3''']pentacene).

couple two Ru LA units through an extended aromatic BL and are of the form $[(phen)_2Ru(tatpp)Ru(phen)_2]^{4+}$, where tatpp = 9,11,20,22-tetraazatetrapyrido[3,2-a:2'3'-c:3",2"-/:2''',3''']pentacene), Figure 1.9. Essential to complex functioning is the electronic isolation of the two Ru LA units coupled with the extended π conjugated ligand. Electronic isolation allows for both Ru LAs to undergo MLCT to the same ligand. This complex functions by optical excitation into a phen type orbital on the BL followed by electron transfer to a lower lying secondary π* acceptor orbital that collects the reducing equivalents. Photolysis of $[(phen)_2Ru(tatpp)Ru(phen)_2]^{4+}$ in the presence of triethylamine, an electron donor, leads to the four electron reduced complex, collecting electrons on the polyazine BL unit.

Bocarsly has studied a series of interesting Pt(IV), centered trimetallic complexes of the form $[(NC)_5M^{II}(CN)Pt^{IV}(NH_3)_4(NC)M^{II}(CN)_5]^{4-}$ (M = Fe, Ru, or Os) that undergo photoinitiated electron collection due to the strong electronic coupling of the LA metal centers. Absorption of one photon of light for the complex M = Fe, results in a net two electron transfer to the central Pt^{IV} followed by cleavage of the polymetallic complex into

two Fe^{III} moieties and a reduced Pt^{II} monometallic complex. These complexes are the first to show photoinitiated electron collection to a metal center.

Nocera designed the complex, $[Rh_2^{0,0}(dpfma)_3LL']$ where dfpma is bis(difluorophosphino)methylamine (a bridging ligand), L = PPh_3, L' = CO uses two electron mixed-valency to drive multi-electron photochemistry. UV-Vis photolysis of $[Rh_2^{0,0}(dpfma)_3LL']$ in 0.1M HCl/THF, results in photolabilization of CO and coordination of 2 equiv. of halide with concurrent H_2 evolution, $[Rh_2^{0,II}(dpfma)X_2] + H_2$. Further photolysis in the presence of a halogen trap such as THF regenerates the catalytically active species $[Rh_2^{0,0}(dpfma)_3L]$. This represents the first example of multi-electron photochemistry being used to drive hydrogen production.

Recently Brewer reported the modification of a previously studied trimetallic complex, $[\{(bpy)_2Ru(dpb)\}_2IrCl_2](PF_6)_5$. The new complex utilized a Rh metal center with lower energy dσ* orbitals and dpp BLs with higher energy π* acceptor orbitals (dpp = 2,3-bis(2-pyridyl)pyrazine). The resulting complex, $[\{(bpy)_2Ru(dpp)\}_2RhCl_2](PF_6)_5$, coupled two Ru LAs through polyazine BLs to a central Rh core. The result produced the first functioning photoinitiated electron collector with collection of reducing equivalents on the metal center and with the supramolecular assembly remaining intact following electron collection.

The complex $[\{(bpy)_2Ru(dpp)\}_2RhCl_2](PF_6)_5$ has recently been shown to function as a device for photocatalytic hydrogen production from water using dimethylaniline as an electron donor. Also, this complex is the focus of the present work with respect to LED device application.

Homogeneous photocatalytic hydrogen production reactions are complex. In order to understand photocatalytic systems it is necessary to vary the nature of the LA, CAT, BL, and ED. It is also important to understand such factors as the impact of pH, ionic strength, solvent, wavelengths of light, intensity of light and temperature. Conventional photochemistry is done using a single light source and performing one experiment at a time. The factors which impact photochemical hydrogen production are numerous, and a method of investigation is needed that allows for studying multiple perturbations simultaneously.

1.2.9 Light Emitting Diodes (LEDs)

The ability to provide stable and reproducible light is key to any successful photochemical system. Contemporary photochemistry utilizes lamps such as Xe arc lamps for photochemical experiments. These lamps mimic solar emission including ultra-violet, visible, and infrared radiation. Conventional lamps are usually filtered to achieve the desired wavelength range. Investments must be made in the lamp and suitable filters to provide excitation options in experimentation. Light emitting diodes (LEDs) offer a low cost alternative as a light source. LEDs have low power consumption, long lifetimes, and fast response.

LEDs are solid state devices consisting of p and n type semiconductors. In a p-type semiconductor the bulk material, germanium for example, is doped with an electron deficient dopant such as gallium. The electropositive dopant provides low energy acceptor orbitals (holes) which, when populated by the valence band, allow for

conduction. Similarly, in an n-type semiconductor, the bulk material, again germanium for example, is doped with an electronegative dopant such as arsenic. The electronegative dopant carries high energy electrons relative to the valence band. The high energy electrons allow for population of the conduction band of the bulk material, Figure 1.10A.[6] Light emitting diodes consist of p and n type semiconductors junctioned together. A depletion zone forms between the semiconductors as a result of charge recombination, Figure 1.10B. The energy difference between the valence band and conduction band is known as the band gap. When a forward bias is applied current

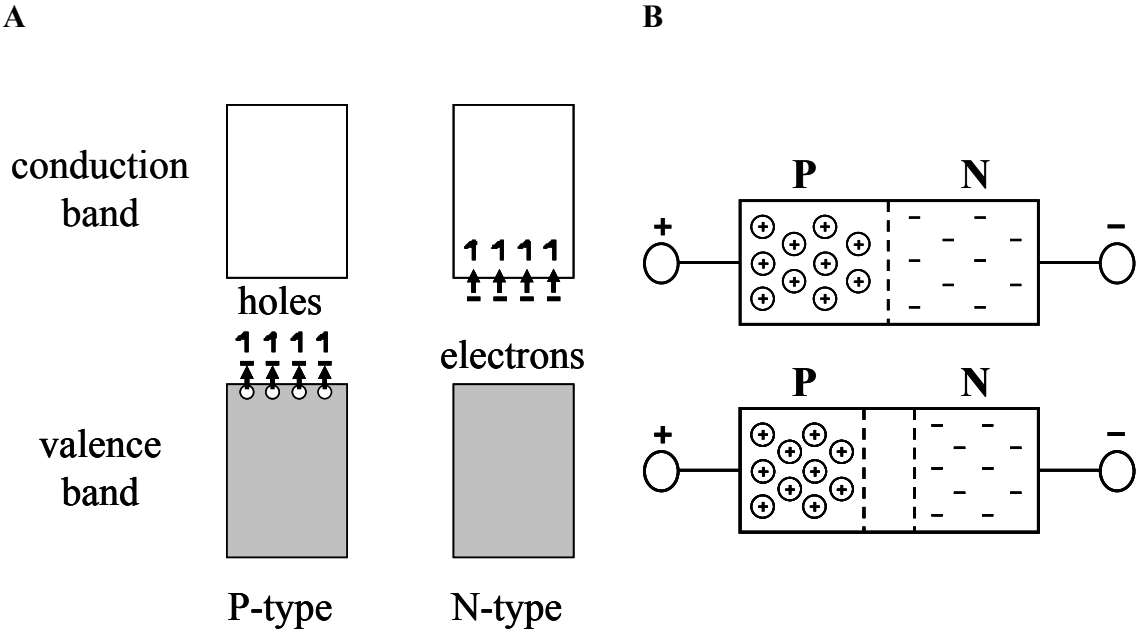

Figure 1.10 A. Schematic representation of p and n type semiconductors. **B** A depletion layer develops concurrent with p and n junctioning (bottom)

passes across the depletion zone. The applied potential supplies enough energy to promote electrons into the conduction band. The electrons are not stable in this excited state and return to the ground state with concurrent energy loss. If the band gap is between 1.55-3.10 eV much of the energy lost is given as light. The band gap and therefore the light emitted, may be tuned by varying the identity and proportions of the dopants used. LED's became commercially available in the late 1960's. Most LEDs are made from GaP (540 nm), GaAs (890 nm), or a mixture of the two.[15] Blue LEDs, GaN (365 nm) were not commercially available until 1984,[15] and it was not until 1993 that they were made with comparable outputs to other LEDs. Kahn recently developed a deep UV LED emitting at 285 nm, which is currently marketed by Sensor Electronic Technology, Inc.[16] Phillips Lumileds Lighting Company developed the first high power LEDs (1 W, 350 mA) in 1999. Prior to this all LEDs were powered between 20-50 mA. Phillips Lumileds continued to lead high power LED technology by releasing a line of 5 W, 700 mA LED in 2002, and recently they released a line of 8.3 W, 2000 mA LED.[17] It is important to point out that just in the last five years, the power output and available wavelengths have developed such that LEDs have become attractive as photolysis sources for investigations in solar energy conversion.

1.2.10 LEDs in Research

The use of LEDs in chemical research was first suggested in 1970 by Barnes and in 1973 by Flaschka. The application was as a light source in flow-through cells for electronic absorption spectroscopy. This was realized in 1978 by Betteridge who

constructed a flow-through cell for metal ion detection with ppb sensitivity using a GaP 650 nm LED as the light source, and a phototransistor as the detector. LEDs with light outputs from red to green developed quickly allowing for more options. Dasgupta described an LED flow-through cell coupling multiple LEDs of differing wavelengths through fiber optic cables to enhance LED applications. In a 1980 investigation, Mader assembled an array of 144 30 mA LEDs for irradiance onto a 1 cm cuvette. This array incorporated GaP 650 nm LEDs and boasted a continuous output of 1×10^{18} photons min^{-1}. LEDs have found application in most spectroscopic instrumentation and several reviews are available. Since the late 1990's researches have investigated the effectiveness of LEDs with respect to halogen lamps on curing dentin bonding agents. Several authors have shown that there is no statistically significant difference between LEDs and halogen lamps in the photolysis of the curing agents over equivalent wavelengths with respect to bond strength. LEDs have also begun to replace lasers and Xe arc lamps in applications such as photodynamic therapy. In a recent study it was shown that there was no statistically significant difference between the effectiveness of LEDs as compared to a Xe arc lamp with respect to cell death in photodynamic therapy in the treatment of oral lesions, Figure 1.11. Bernhard recently constructed an eight well LED array for photochemical hydrogen production studies using Ir photosensitizers and a Co catalyst. The LED array was used to optimize system parameters and evaluate the photosensitizers. The successful application of high intensity LEDs in photocatalytic hydrogen production studies shows promise as a method of photochemical research.

A **B**

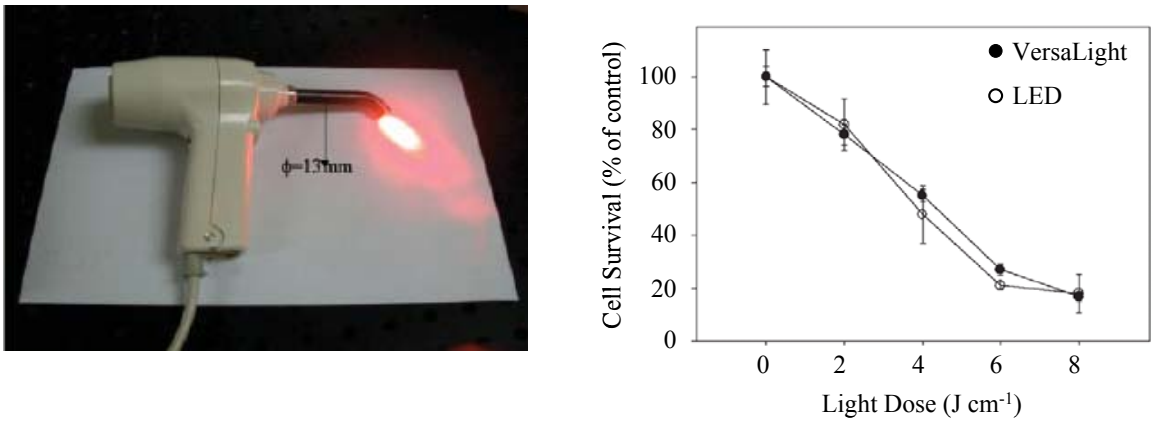

Figure 1.11 A. Custom built LED gun for photodynamic therapy. **B.** 5-Aminolevulinic acid (ALA)-photodynamic therapy (PDT) induced cytotoxicity using different light sources.

However, studies are needed to quantitatively determine the error involved with using LEDs as a high intensity photolysis source. Also, the method of photolysis with high intensity LEDs must be validated with respect traditional methods.

In this research, the design, construction, and evaluation of a series of LED array photolysis systems for high throughput photochemistry have been performed. Three array systems of increasing sophistication are evaluated using calorimetric measurements and potassium tris(oxalato)ferrate(III) chemical actinometry. The LED arrays were compared with a traditional 1000 W Xe arc lamp source in terms of cost, light intensity, and light stability. Two constant current drivers were evaluated with respect to LED array performance. The results are analyzed using descriptive statistics and analysis of variance (ANOVA). The optimized third generation LED array was evaluated as the

photolysis source for photochemical hydrogen production experiments using the supramolecular catalyst $[\{(bpy)_2Ru(dpp)\}_2RhCl_2](PF_6)_5$.

The optimized third generation LED array has been shown to be modular, controllable, cost effective, and comparable in photonic output to a filtered 1000 W Xe arc lamp. The optimized LED array has been shown to produce statistically equivalent light flux for each LED in the array. Constant current drivers have been shown to be inadequate as a power source for an LED array. The optimized third generation LED array has produced statistically equivalent results when used as a high throughput system for solar hydrogen production studies using the supramolecular complex $[\{(bpy)_2Ru(dpp)\}_2RhCl_2](PF_6)_5$.

Chapter 2. EXPERIMENTAL

2.1 Materials

All materials were used without further purification. Potassium tris(oxalato)ferrate(III) was purchased from Strem Chemicals, Inc. (Newburyport, MA). Sulfuric acid (~38 N), dimethylformamide, acetone, 2,2'-bipyridine (bpy), 2,3-bis(2-pyridyl)pyrazine (dpp), 1,10-phenanthroline, lithium chloride, potassium hexafluorophosphate, and sodium acetate were purchased from Sigma-Aldrich, Inc. (St. Louis, MO). Burdick and Jackson UV-Vis grade acetonitrile was purchased from VWR International. The argon used was purchased from Airgas, Inc. (Radnor, PA). The 1000 W Xe arc lamp, NIR water filter, 460 ± 5 nm peak width at half height (FWHM) interference filter, and optical rail were purchased from Newport Corporation – Oriel Products (Stratford, CT). Sample cells used in photochemical experiments with the Xe arc lamp were purchased from Starna Cells, Inc. (Atascadero, CA). Photolysis cells used in the LED array experiments were constructed locally. Aluminum materials used for LED array housing were gifted (scrap) from the University Machine Shop (Virginia Tech).

All electronic components used in the construction of LED arrays are presented in Table 2.1. These components were used according to manufacturer's guidelines for power and thermal management. Prolight Opto Technology Corporation (Taoyuan Hsien, Taiwan, R.O.C) is the manufacturer of the Prolight 5 W LEDs distributed by Stellatus

Lighting LTD (Clydebank, United Kingdom). Philips Lumileds Lighting Company (San Jose, CA) is the manufacturer of the Luxeon V 5 W LEDs distributed by Future Electronics (Pointe-Claire, Quebec).

Table 2.1 Electronic components used in construction of the LED arrays

Distributor	Description	Part Number	Price[f]
Stellatus Lighting LTD[a]	White 5 W Star LED	PG1N-5LWS	16.00
Stellatus Lighting LTD	Warm White 5 W Star LED	PG1N-5LVS	16.00
Stellatus Lighting LTD	Blue 5 W Star LED (470 nm)	PG1N-5LGS	16.00
Stellatus Lighting LTD	Green 5 W Star LED (530 nm)	PG1N-5LBS	16.00
Stellatus Lighting LTD	Amber 5 W Star LED (590 nm)	PG1N-5LAS	16.00
Stellatus Lighting LTD	Orange 5 W Star LED (617 nm)	PG1N-5LHS	16.00
Stellatus Lighting LTD	Red 5 W Star LED (625 nm)	PG1N-5LRS	16.00
Stellatus Lighting LTD	Reflector	PG1N-RY10	2.00
Future Electronics[b]	Royal-Blue 5 W Star LED (455 nm)	LXHL-LR5C	12.70
Future Electronics	Blue 5 W Star LED (470 nm)	LXHL-LM5C	12.70
Future Electronics	Cyan 5 W Star LED (505 nm)	LXHL-LM5C	12.70
Future Electronics	Green 5 W Star LED (530 nm)	LXHL-LM5C	12.70
Future Electronics	Xitanium Driver (17 W, 700 mA)	LED120A0700C24F	15.52
Future Electronics	Xitanium Driver (25 W, 1050 mA)	LED120A0024V10F	27.45
Newark InOne[c]	Heat Sink (LEDs, 7.5 Ohm Resistor)	96C7858	1.26
Newark InOne	Heat Sink (Resistors)	14C3686	1.23
Newark InOne	2 Ohm Resistor (10 W, ± 1 %)	825F2R0	4.00
Newark InOne	5 Ohm Resistor (10 W, ± 1 %)	64K9744	2.83
Newark InOne	7.5 Ohm Resistor (10 W, ± 1 %)	01F9754	2.68
Newark InOne	10 Ohm Resistor (10 W, ± 1 %)	91F5357	2.83
Newark InOne	25 Ohm Rheostat (25 W, 1 turn)	01F7552	27.13
Jameco Electronics[d]	Power Supply (13.8 V DC, 96.6 W)	136581CB	59.95
Jameco Electronics	Terminal Block (10 A @ 600 V)	208899CX	2.39
Jameco Electronics	Toggle Switch (SPDT On-Off-On)	318140CB	2.89
Newegg.com[e]	Fan (32.5 CFM, <20 dBA)	N82E16835119033	7.49
Newegg.com	Heat Sink Cement	N82E16835100005	10.99

[a]Stellatus Lighting LTD (Clydebank, United Kingdom; www.led-bulbs.com). [b]Future electronics (Pointe-Claire, Quebec; www.futureelectronics.com). [c]Newark InOne (Chicago, IL; www.newark.com). [d]Jameco Electronics (Belmont, CA; www.jameco.com). [e]Newegg.com (Industry, CA). [f]Prices in USD for August 2006

2.2 Characterization Techniques

2.2.1 Electrochemistry

A Bioanalytical Systems, Inc. 100W electrochemical analyzer was used for all electrochemical experiments. The supporting electrolyte was 0.1 M Bu_4NPF_6. The measurements were made in Burdick and Jackson UV-grade acetonitrile. Cyclic and square wave voltammetry experiments were carried out using a three electrode cell, which uses a 1.9 mm platinum disk working electrode, a platinum wire auxiliary electrode, and an Ag/AgCl reference electrode (0.29 V vs. NHE). The Ag/AgCl reference electrode was calibrated against the $FeCp_2/FeCp_2^+$ couple (0.67 V vs. NHE).[18] The platinum electrode was polished with 0.05 μm alumina between each scan. The analyte solution was deoxygenated by bubbling with argon for 10 min.

2.2.2 Electronic Absorption Spectroscopy

Solution spectra were recorded at room temperature using a Hewlett Packard 8452A diode array spectrophotometer, with 2 nm resolution and a detection range from 190 to 820 nm. The solvent used was Burdick and Jackson UV-grade acetonitrile. Measurements were made using either 1 cm or 0.2 cm path length quartz cuvettes. Spectra were recorded for purposes of characterization as well as to determine catalyst concentrations in the photochemical hydrogen production experiments. The concentration of the catalyst $[\{(bpy)_2Ru(dpp)\}_2RhCl_2](PF_6)_5$ in the hydrogen production experiments was determined according to Beer's law using the previously published

molar extinction coefficient (ε = 20100 M^{-1} cm^{-1}) that corresponds to the Ru(dπ)→dpp(π*) MLCT transition occurring at 514 nm.[19]

2.2.3 Irradiance Spectroscopy

The spectral output of the LEDs used in the present work was determined by measuring the relative irradiance of each LED using an Ocean Optics diode array spectrophotometer with 0.2 nm resolution and a detection range from 178 to 890 nm. The measurement was taken as follows: In a dark room the LEDs were powered and the relative irradiance measured by aligning the fiber optic lead to the spectrophotometer. The distance between the LED and the fiber optic was such that the peak relative irradiance was 70 % of the maximum observable value. The measurement is shown in Figure 2.1

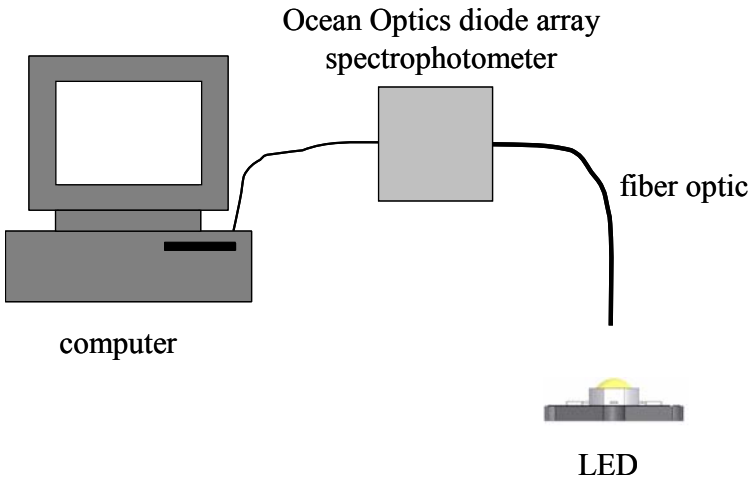

Figure 2.1 The fiber optic sensor lead from an Ocean Optics diode array spectrophotometer oriented towards the LED for relative irradiance measurement. Determination of the relative spectral irradiance was performed in a dark room with the only light being the LED.

2.2.4 Emission Spectroscopy

Solution spectra were recorded at room temperature from deoxygenated solutions using a Photon Technology Inc. (PTI) modified quanta master model QM-200-45t spectrofluorometer equipped with a water-cooled 150 watt Xe arc lamp excitation source. The monochromator has 0.2 nm resolution. The detector used was a Hamamatsu 1527 photomultiplier tube (PMT) contained in a Products for Research thermoelectrically cooled single photon counting system.

2.2.5 Physical Actinometry

An actinometer is a chemical system or physical device that allows for the determination of the number of photons into a defined space integrally or per unit time. In physical actinometry the interaction of electromagnetic radiation with a light sensitive device such as a photodiode, thermopile, or photomultiplier results in a change that affords a potential.[20] The potential can then be measured and calibrated to provide accurate determination of photon flux. The physical method chosen for determining the irradiance onto a sensor was calorimetry.

The calorimetric measurements were made with a Scientech, Inc. (Boulder, CO) Mentor MA 10 with a MC2501 calorimeter head unit. The measurements are made by centering the calorimeter head unit over each photolysis well and measuring the radiant energy of the light emitted through the aperture by the LED. Figure 2.2. Figure 2.3A[21] is a schematic of a calorimeter head unit containing a black disk absorber coupled to a thermopile sensor.

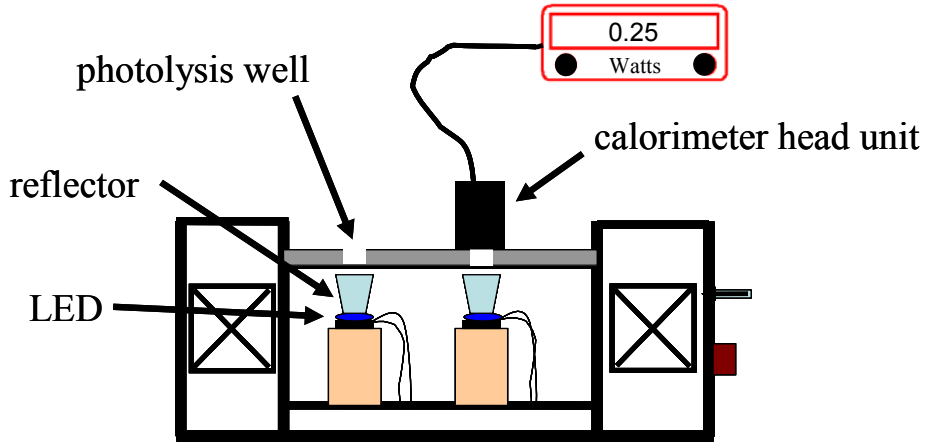

Figure 2.2 Schematic representation of a calorimetric measurement using the 3rd generation LED array.

As light propagates through the head unit aperture the black disk absorbs all radiant energy and transfers this energy to the thermopile sensor. The calorimeter functions by use of a thermopile. A schematic of the thermopile is shown in Figure 2.3B. The thermopile contains a series of P-N semiconductor junctions which are connected electrically in series. Electron hole pairs, which are thermally induced at P-N junctions, produce a current that is proportional to the radiant energy that impinges on the black disk absorber.

Thermopiles measure average energy per unit time onto the disk absorber. This measurement is often reported in Watts, equation 2.1. As such, photon flux can be determined from a calorimetric measurement if the spectral output of the light source measured is known.

$$W = \frac{J}{s} \tag{2.1}$$

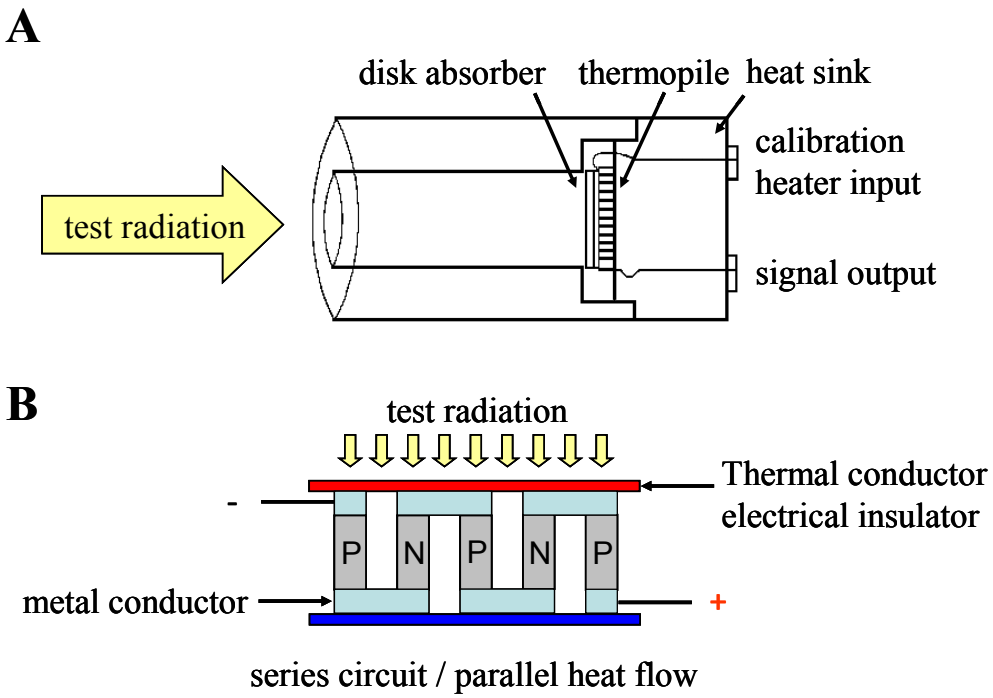

Figure 2.3 Schematics of **A.** calorimeter head unit and **B.** a thermopile.

As LEDs are not monochromatic, determining the photon flux from a calorimetric measurement requires integrating the energy of the emitted light, Figure 2.4. First, the total area of the spectral output was calculated in Excel from the exported Ocean Optics spectral irradiance data using the right endpoint approximation. The step size was 0.2 nm, equation 2.2. In calculating the total area I is the intensity in counts, λ is the wavelength given in nm and n refers to the individual measurements.

$$\text{Total Area} = \sum [I_{n+1}(\lambda_{n+1} - \lambda_n)] = 1.87 \times 10^6 \qquad (2.2)$$

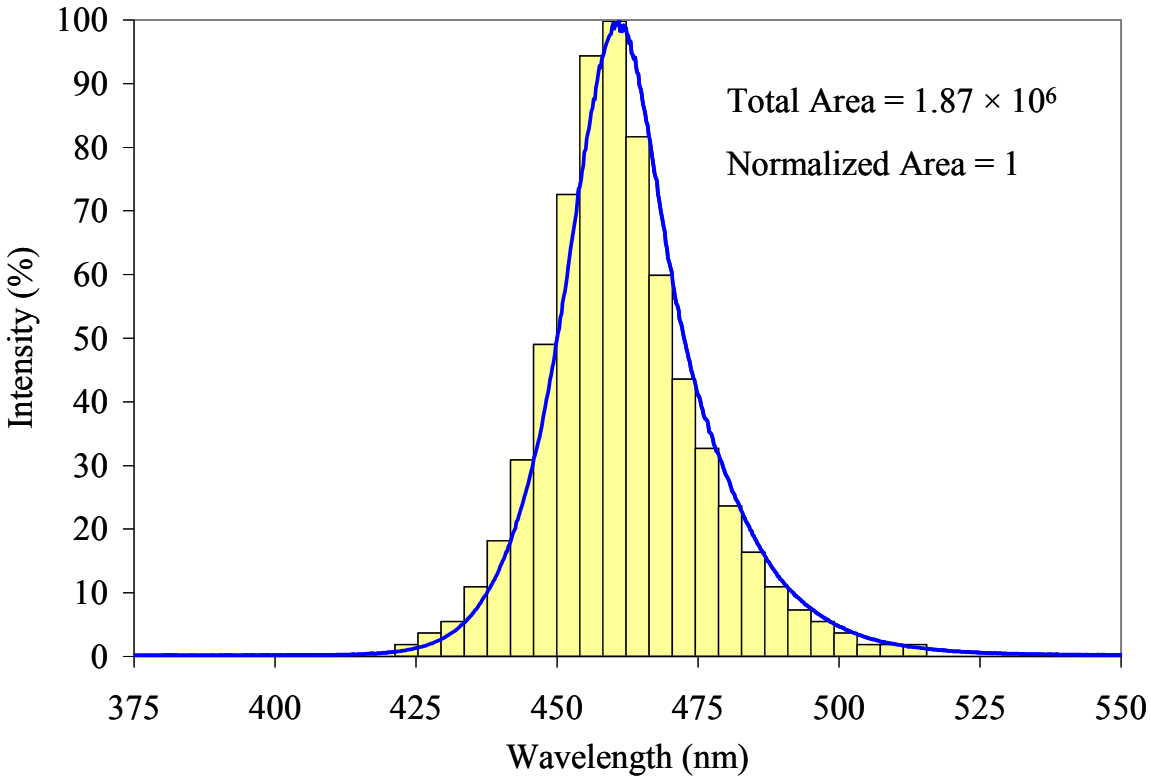

Figure 2.4 LED spectral output with rectangles overlaid representing the right endpoint approximation determining area. The step size used was 0.2 nm.

The spectral output was then normalized to 1 allowing each rectangle to represent a normalized fraction per wavelength, f_n, of the total area, equation 2.3. An example of this calculation is shown in equation 2.4 for the datum collected at 462.8 nm, $I_{462.8}$ = 59349.59.

$$f_n = \left[\frac{I_{n+1}(\lambda_{n+1} - \lambda_n)}{\sum [I_{n+1}(\lambda_{n+1} - \lambda_n)]} \right] \tag{2.3}$$

$$f_{462.8} = \left[\frac{(59349.59\ counts)(462.8\ nm - 462.6\ nm)}{1.870 \times 10^6\ counts \cdot nm} \right] = 6.347 \times 10^{-3} \tag{2.4}$$

The fractional energy, J_n, was then calculated by multiplying the normalized fraction per wavelength, f_n, by the energy per wavelength, equation 2.5. An example is given in equation 2.6. The total energy contained in the spectral output, J_{total}, is then calculated, equation 2.7

$$J_n = hc\frac{f_n}{\lambda_n} \tag{2.5}$$

$$J_{462.8} = (6.626\times10^{-34} J\cdot s)(2.998\times10^{8} m\cdot s^{-1})\left(\frac{6.347\times10^{-3}}{4.628\times10^{-7} m}\right) = 2.724\times10^{-21} J \tag{2.6}$$

$$J_{total} = hc\sum\frac{f_n}{\lambda_n} = 4.280\times10^{-19} J \tag{2.7}$$

Finally, the photon flux, q_p, can be determined by dividing the measured light energy J_{meas} by the total energy from the LED emission profile, J_{total}, equation 2.8.

$$q_p = \frac{J_{meas}}{J_{total}} = \frac{0.240\, W}{4.280\times10^{-19} J} = 5.61\times10^{17}\ photons\cdot s^{-1} \tag{2.8}$$

2.2.6 Chemical Actinometry

Chemical actinometry is a technique used to quantify the irradiance into a sample cell by a light source. Actinometry uses a photochemical reaction that has a known mechanism and a known quantum yield, Φ, of product formation. Quantum yield for the tris(oxalato)ferrate(III) chemical actinometer refers to the ratio of the photolysis product formed to the number of quanta absorbed by the actinometer at the wavelength of photolysis, equation 2.9. Chemical actinometry was performed by using the potassium

$$\Phi_{Fe^{+2}} = \frac{moles \quad Fe^{+2} \quad formed}{einsteins \quad of \quad light \quad absorbed} \tag{2.9}$$

tris(oxalato)ferrate(III) chemical actinometer. The mechanism of ferrioxalate photoreduction is given in equations 2.10-2.11, with the net chemical reaction shown in equation 2.12.[22-26]

$$[Fe(C_2O_4)_n]^{(3-2n)} \xrightarrow{h\nu} Fe^{2+} + (n-1)C_2O_4^{2-} + C_2O_4^{-} \tag{2.10}$$

$$C_2O_4^{-} + [Fe(C_2O_4)_n]^{(3-2n)} \rightarrow Fe^{2+} + nC_2O_4^{2-} + 2\ CO_2 \tag{2.11}$$

net: $$2\ [Fe(C_2O_4)_n]^{(3-2n)-} \xrightarrow{h\nu} 2\ Fe^{2+} + (2n-1)C_2O_4^{2-} + 2\ CO_2 \tag{2.12}$$

The mechanism is written suggesting the equilibrium between mono, bis, and tris oxalato complexes present at the pH of the actinometry solutions.[26,27] According to the mechanism it can be seen that absorption of one photon results in reduction at the Fe center and decomposition to give oxalate ion and oxalate radical ion. The oxalate radical ion then reacts with $[Fe(C_2O_4)_n]^{(3-2n)}$ causing reduction at another Fe center and decomposition to give oxalate ion and carbon dioxide. The sum of equations 2.10 and 2.11 show that absorption of one photon yields two ferrous ions. The backward component of reaction 2.11 is negligible at the conditions used for actinometry.[24] Also, the photolysis products do not appreciably absorb light of the same energy as $[Fe(C_2O_4)_3]^{3-}$.[22] The concentration of Fe^{2+} produced is determined spectrophotometrically by the formation of $[Fe(phen)_3]^{2+}$ by complexing Fe^{+2} with 1,10-phenanthroline, which has a strong absorption at 510 nm.[20,26] The incident radiation can then be determined by the ratio of the moles of Fe^{+2} formed, shown in equations 2.10-2.11, to the product of the quantum yield of formation Fe^{+2} at the wavelength of

Table 2.2 Quantum yield of the ferrioxalate actinometer at 22°C.[28]

Wavelength (nm)	Quantum Yield, Φ_{Fe}^{2+}
577	0.013
546	0.15
509	0.86
480	0.94
468	0.93
436	1.01
405	1.14
365	1.18

photolysis and the photolysis time. Table 2.2 lists a summary of quantum yield values, Φ_{Fe}^{2+}.[28] All actinometry experiments were conducted in the dark with a 630 nm Prolight 5 W LED as a working light.

Actinometry was performed in the second and third generation array systems as follows: Two solutions were prepared, the actinometer solution, and the developing solution. The actinometer solution was prepared by combining 7.37 g, 15.0 mmol $K_3Fe(C_2O_4)_3 \cdot 3H_2O$ with 10.0 mL of 1.00 N H_2SO_4 in a 100 mL volumetric flask, and diluting to 100.00 mL with deionized water (DI H_2O). An 8.50 mL aliquot of the gravimetrically determined 0.150 M $K_3[Fe(C_2O_4)_3]$ solution was then transferred into a locally constructed gas tight cell. Figure 2.5A represents a spectrum of the actinometer solution, 0.150 M $[Fe(C_2O_4)_3]^{3-}$, 0.0500 M H_2SO_4, taken at room temperature in a 1 cm cell. The second generation LED array utilizes flat bottomed optical quality 16 (O.D) mm × 50 mm cylindrical glass cells, which were septum capped. The third generation LED array utilizes a flat bottomed optical quality 22 (O.D) mm × 30 mm cylindrical glass

septum capped cell. The cells were septum capped and photolyzed for 1 min while bubbling with argon. A 5.5 mL aliquot of the photolyzed solution was then transferred into a 25.00 mL volumetric flask along with a 4.0 mL aliquot of saturated aqueous 1,10-phenanthroline solution, which has a literature value of 16.1 mM,[29] and a 10.0 mL aliquot of 0.6 M $NaCH_3COO$, 0.18 M H_2SO_4 buffer solution. The flask was brought to 25.00 mL total volume using DI H_2O. This solution was allowed to react one hour in the dark, then analyzed using electronic absorption spectroscopy. The spectra were evaluated at 510 nm to determine the $[Fe(phen)_3]^{2+}$ complex concentration. Figure 2.5B represents a spectrum of the actinometer solution after reaction with 1,10-phenanthroline. The top spectrum in Figure 2.5B was photolyzed for 1 min with a 470 nm LED. The bottom spectrum was a dark control. The spectra were taken at room temperature in 0.2 cm cells. A blank was also used for comparison by following the aforementioned process without photolysis. The blank was kept on the workbench for the duration of the experiment. The actinometry experiments were also done with a 1000 W Xe arc lamp. These experiments were done in the same manner as the second and third generation LED array systems with the following modifications. A 12.2 mL aliquot of 0.15 M $K_3[Fe(C_2O_4)_3]$ was dispensed into a 10 (O.D.) mm × 50 mm cylindrical gas tight, septum capped cell and photolyzed for two minutes while deoxygenating with argon. The remaining procedure was carried out as detailed above. It is important that the photolysis does not result in greater than 5% conversion, as the production of the photoproduct results in a diminished

A

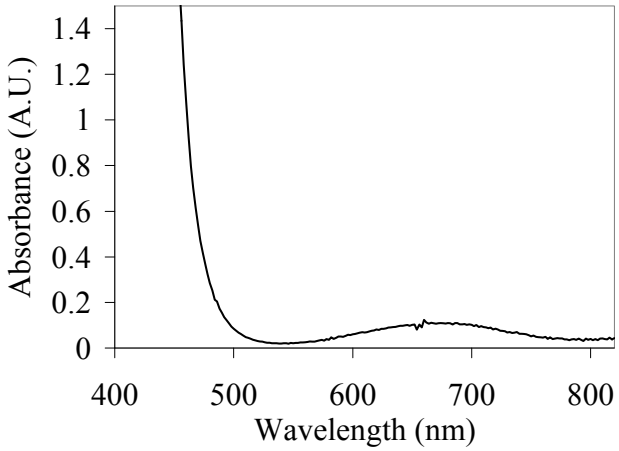

B

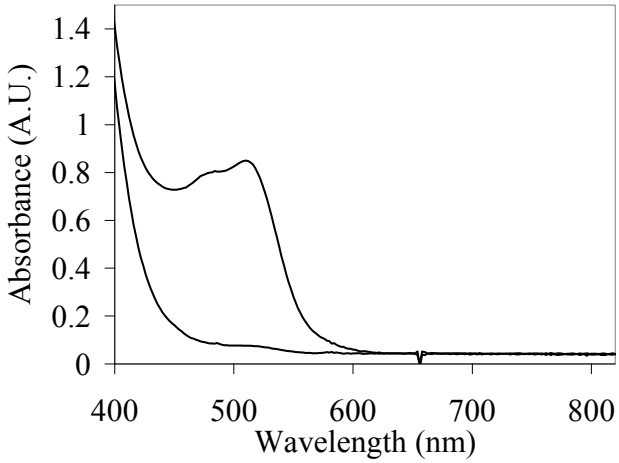

Figure 2.5 Electronic absorption spectrum of ferrioxalte actinometer **A.** Before photolysis[a] and **B.** after photolysis and development[b].
[a]Aqueous solution recorded at room temperature in a 1 cm cell, 0.15 M $[Fe(C_2O_4)_3]^{3-}$, 0.05 M H_2SO_4.
[b]Two aqueous solutions after reaction with 1,10-phenanthroline, 0.15 M $[Fe(C_2O_4)_3]^{3-}$, 0.05 M H_2SO_4. The spectrum displaying the larger 510 nm absorbance was photolyzed for 1 min with a 470 nm Luxeon V LED, and the spectrum displaying the smaller 510 nm absorbance was kept in the dark as a control. Aliquots of the actinometer solutions were combined with 1,10-phenanthroline and acetate buffer to give final solutions of 33 mM $[Fe(C_2O_4)_3]^{3-}$, 2.58 mM 1,10-phenanthroline, 240 mM $NaCH_3CO_2$, 72 mM H_2SO_4. The spectra were obtained after the combined solutions were allowed to react in the dark for a period of 1 hr.

absorbance at the wavelengths of photolysis, as well as an accumulation of $Fe(C_2O_4)$, which precipitates out of the solution.[22] Also, the actinometer solutions should be made fresh before experimentation as aqueous solutions of $K_3[Fe(C_2O_4)_3]$ and 1,10-phenanthroline are extremely light sensitive.[20,30]

The number of Fe^{2+} atoms, Fe^{2+}, was calculated using equation 2.13

$$n_{Fe^{2+}} = \frac{6.023\times10^{23} V_1 V_3 (A_E - A_D)}{V_2 l \varepsilon} \quad (2.13)$$

where V_1 is the photolysis volume, V_2 is the volume of irradiated solution used for analysis, V_3 is the volume to which V_2 was diluted, A_E is the absorbance of the analyzed solution after photolysis, A_D is the absorbance of the analyzed dark control solution, l is the path length of the cell used for spectrophotometric determination, and ε is the molar extinction coefficient of $[Fe(phen)_3]^{2+}$ is approximately equal to 1.11×10^4 L mol^{-1} cm^{-1}. An example is shown in equation 2.14. The example shown is taken from an actinometry experiment using the 3rd generation LED array where V_1 = 8.50 mL, V_2 = 5.50 mL, V_3 = 25.00 mL, l = 0.2 cm, AE and AD are taken from data presented in Figure 2.5B.

$$n_{Fe^{2+}} = \frac{(6.023\times10^{23})(0.00850\ L)(0.02500\ L)(0.850296\text{-}0.0759888)}{(0.00550\ L)(0.200\ cm)(1.11\times10^{4}\ L\cdot mol^{-1}\cdot cm^{-1})} = 8.12\times10^{18} \quad (2.14)$$

The error obtained in the present study is in agreement with literature values, and is generally ± 2-5 %.[31] The photon flux, q_p, into the sample cell is calculated by relating the quantum yield of product formation to the rate of product formation according to equation 2.15.

$$q_p = \frac{n_{Fe^{2+}}}{\Phi_{Fe^{2+}} \cdot t} \tag{2.15}$$

The quantum yield of formation for Fe^{2+}, $\Phi_{Fe}{}^{2+}$, is 0.93 when photolyzed at 468 nm, and the reaction time, *t*, is given in min. The example is continued in equation 2.16.

$$q_p = \frac{8.12 \times 10^{18}}{0.93 \cdot 1.0\,\text{min}} = 8.8 \times 10^{18}\ photons \cdot \text{min}^{-1} \tag{2.16}$$

2.3 Synthesis

2.3.1 $[Ru(bpy)_2Cl_2]$

This complex is commercially available as $[Ru(bpy)_2Cl_2]\cdot 2H_2O$ CAS number: 15746-57-3. The synthesis of $[Ru(bpy)_2Cl_2]$ was according to a previously published procedure.[32] LiCl (8.43 g, 199 mmol), 2,2'-bipyridine (9.36 g, 60.0 mmol), and $RuCl_3\cdot 3H_2O$ (7.80 g, 38.0 mmol) were combined in dimethylformamide (50.0 mL) in a 250 mL round bottom flask. The mixture was heated at reflux, under an argon atmosphere with stirring for 8 hr. During this time the solution changed in color from red-brown to dark purple. The solution was allowed to cool to room temperature, and added to 250 mL of acetone in a 500 mL Erlenmeyer flask. The solution was placed in the freezer to induce precipitation. The black precipitate was filtered by vacuum filtration, and washed with several portions deionized water in order to remove excess LiCl, $RuCl_3\cdot 3H_2O$, and $[Ru(bpy)_3]Cl_2$, which is the major impurity formed. The product was dried in a vacuum desiccator. Yield: 50 %, 8.24 g, 17.0 mmol.

To ensure removal (ppm) of $[Ru(bpy)_3]^{2+}$ which forms as a byproduct during the course of the reaction, the product was rinsed with large volumes of deionized water. The washings were monitored by emission spectroscopy by exciting at 436 nm and monitoring the emission over the range of wavelengths from 500–800 nm. $[Ru(bpy)_3]^{2+}$ is water soluble and has a strong emission at 620 nm ($\Phi_{em} = 4.0 \times 10^{-2}$).[33] Generally, this procedure required several washings with DI H_2O to obtain the desired purity.

2.3.2 $[(bpy)_2Ru(dpp)](PF_6)_2$

The synthesis of $[(bpy)_2Ru(dpp)](PF_6)_2$ was according to a previously published literature procedure.[32] 2,3-bis(2-pyridyl)pyrazine (1.46 g, 6.24 mmol), $[Ru(bpy)_2Cl_2]$ (2.07 g, 4.28 mmol), and 2:1 ethanol/water (90.0) mL were combined in a 250 mL round bottom flask. The mixture was heated at reflux for 3 hr. The product was flash precipitated by the addition of the reaction mixture to saturated aqueous KPF_6 (approximately 400 mL). The product was isolated by vacuum filtration and dried in a vacuum desiccator. The crude product was purified by column chromatography on alumina with a 3:2 toluene/acetonitrile eluent. The column used was 3.2 (O.D.) × 80 cm with a coarse ground frit. The column was wet-packed by filling it 75 % with solvent prior to adding the alumina. Sea sand was then added slowly and allowed to pack a ~0.5 cm bed. Adsorption alumina 80-200 mesh, which had been deactivated with methanol, was slowly added to form a packing ~25 cm high. Finally, sea sand was then added again in the amount of ~0.5 cm on top of the alumina. The solvent was eluted to the level of the sand and the complex was introduced onto the column in a concentrated form with

no more than ~5 mL added. The desired product is an orange band, which elutes first, followed by a purple by-product band [{$(bpy)_2Ru$}$_2$(dpp)]$(PF_6)_4$. The purple band elutes very slowly allowing for efficient separation; however chromatography was repeated 2-3 times to ensure purity. Yield: 43 %, 1.72 g, 1.84 mmol.

2.3.3 [{$(bpy)_2Ru(dpp)$}$_2RhCl_2$]$(PF_6)_5$

The synthesis of [{$(bpy)_2Ru(dpp)$}$_2RhCl_2$]$(PF_6)_5$ was according to a previously published literature procedure.[32] [$(bpy)_2Ru(dpp)$]$(PF_6)_2$ (0.315 g, 0.336 mmol), $RhCl_3 \cdot 3H_2O$ (0.0450 g, 0.215 mmol) were combined with 15 mL of 2:1 ethanol/water in a one neck 100 mL round bottom flask. The mixture was heated at reflux with stirring for 1 hr. The product was then flash precipitated by the addition of the reaction mixture to saturated aqueous KPF_6 (approximately 100 mL). The crude product was isolated using vacuum filtration, and dried in a vacuum desiccator. The product was purified by recrystallization from hot ethanol. Yield 50 %, 133 g, 0.108 mmol

2.4 Construction of LED Arrays

LED arrays were constructed and evaluated for the purposes of determining a valid method for high-throughput photochemistry. The application of such LED arrays once validated is in the study of photochemical hydrogen production catalysts.

2.4.1 First Generation LED Array

The LED array used in this experiment was a modified version of that implemented by Bernhard et. al[34]. The circuit diagram for the first generation LED array is shown in Figure 2.6A. This design incorporated five 470 nm Prolight Opto Technology Corporation LEDs. The LEDs were wired in parallel, using a 2 ohm resistor, which had a ± 1 % tolerance, for power management. The LEDs were properly heat sinked and were permanently mounted to the heat sinks using thermally conductive heat sink cement. The array was powered by a 13.8 V DC precision regulated power supply. A schematic of the first LED array is shown in Figure 2.6B. The array housing was constructed in house and designed so that the sample cells were top loaded into the array and irradiated from the bottom. Sample cells were 16 (O.D.) mm × 50 mm cylindrical glass cells, which were septum capped, and designed with a flat bottom optical surface to reduce light scatter. The spectral output of the 470 nm Prolight Opto Technology Corporation LEDs is shown in Figure 2.7. The relative intensity spectral output was measured with an Ocean Optics diode array spectrophotometer. The LEDs has a maximum output at 460 nm and 20 nm FWHM, in line with the manufacturer's specifications, Appendix.

A

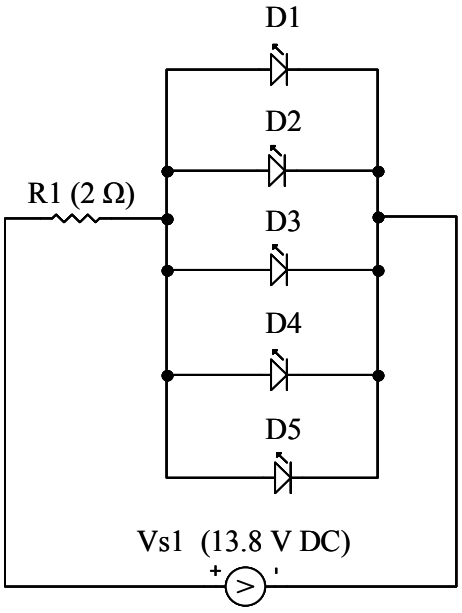

B

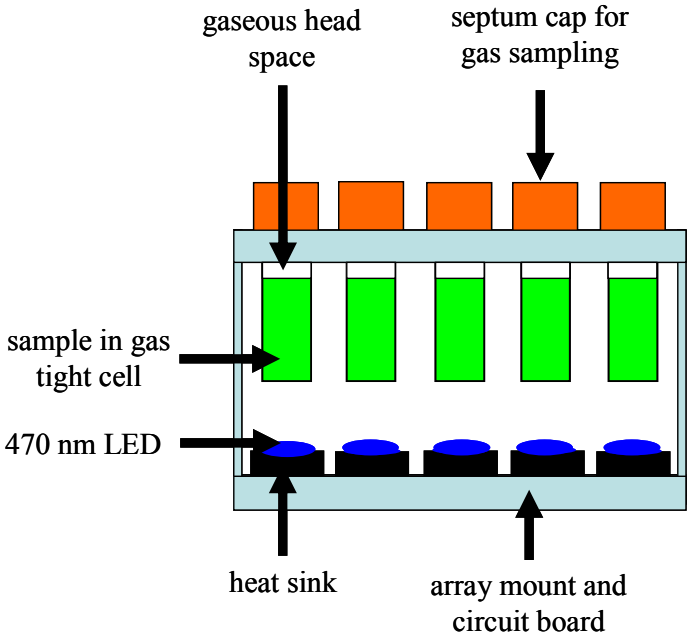

Figure 2.6 A. Circuit diagram of the first generation LED array. In the diagram R1 refers to the 2 ohm resistor and D1-D5 are five 470 nm Prolight Opto Technology Corporation LEDs. Vs1 refers to the 13.8 V DC precision power supply used to power the array. **B.** Schematic of the first generation LED array photolysis system for the photochemical production of H_2 from water using supramolecular catalysts.

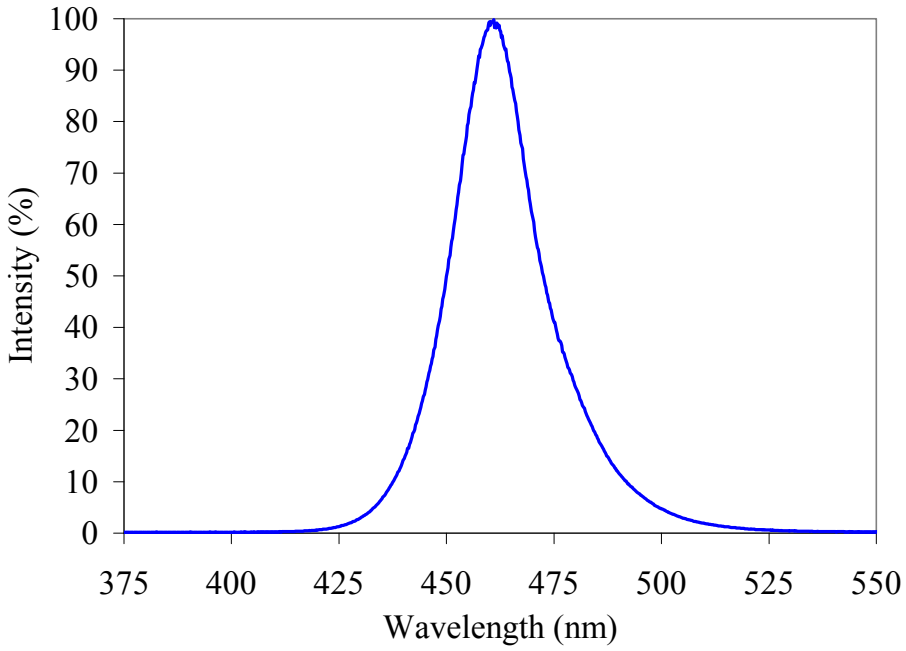

Figure 2.7 LED spectral output of a 470 nm Prolight Opto Technology Corporation LED.

2.4.2 Second Generation LED Array

The circuit diagram for the second LED array is shown in Figure 2.8A. The second generation LED array utilizes the same LEDs and heat sinks as the first array. This design expanded on the 1st generation array by providing a resistor for every LED with power management done in series for every LED in the array. The resistors used in the circuit were 10 ohm resistors, which had a ± 1 % tolerance, and the array was powered by a 13.8 V DC precision regulated power supply. The housing is thermostated to regulate the sample temperature. Sample cells are top loaded into the housing and photolyzed from below. This array uses the same optical cells of local design as the first array.

A

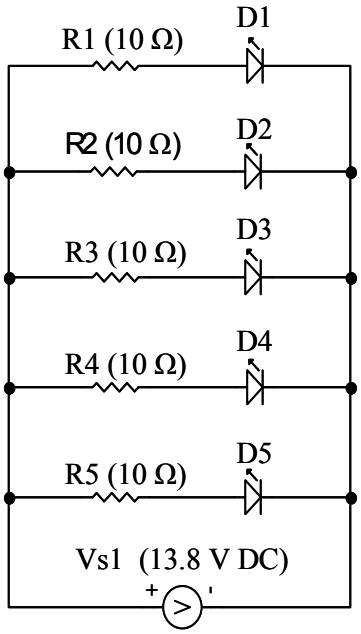

B

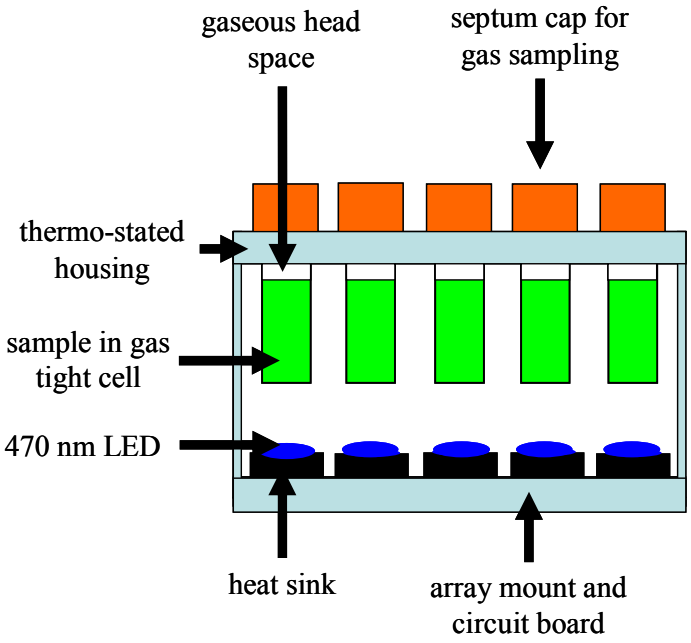

Figure 2.8 A. Circuit diagram of the second generation LED array. In the diagram R1-R5 refer to the 10 ohm resistors and D1-D5 are five 470 nm Prolight Opto Technology Corporation LEDs. Vs1 refers to the 13.8 V DC power supply used to power the array. **B.** Schematic of the second generation LED array photolysis system for the photochemical production of H_2 from water using supramolecular catalysts.

2.4.3 Third Generation LED Array

The third generation array is an optimized design, changing the previous arrays in many ways to improve performance. The circuit diagram for the third generation array is shown in Figure 2.9A. The circuit diagram shown is a truncated version of the operating circuit. It only displays two of the eight LED series-parallel wire runs. In the diagram the rheostats are set at 50 %, which was done for illustrative purposes. In operation, the rheostats would be adjusted as needed. A schematic of the third generation array is shown in Figure 2.10A and a side cut out is shown in Figure 2.10B. In this array all the samples are irradiated from beneath. There is a glass plate attached to the bottom of the thermostated cell holder for cell support. Sample cells are 22 (O.D.) mm × 30 mm cylindrical glass cells, which were septum capped, and designed with a flat bottom optical surface. The cell holder is hinged to allow for easy access to the LEDs. Furthermore, the system is modular in that all the LEDs are interchangeable. Each LED can be turned on or off and the power to each LED can be adjusted. Interchangeable LED units are composed of an LED which is attached to a proper heat sink and mounted to the aluminum base. The base is designed to fit securely into any available housing in the LED chamber. The LED units utilize reflectors which focus the light onto the sample. These reflectors snap onto the LED, but are not rigidly connected and therefore, are interchangeable within the LED unit frameworks. An example LED unit is shown in Figure 2.9B. The array has a single pole double throw (spdt) switch in each series-parallel wire run. This switch has an on-off-on configuration allowing the circuit to accommodate the different power demands of the longer wavelength and shorter wavelength LEDs.

A

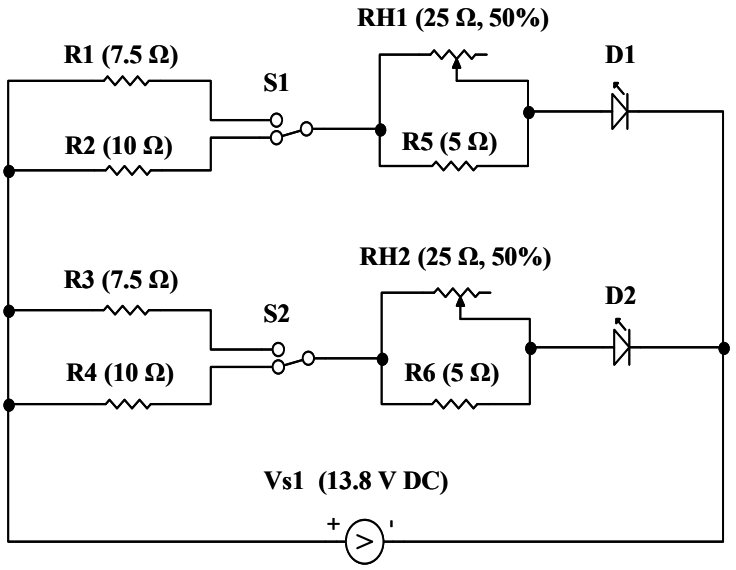

B

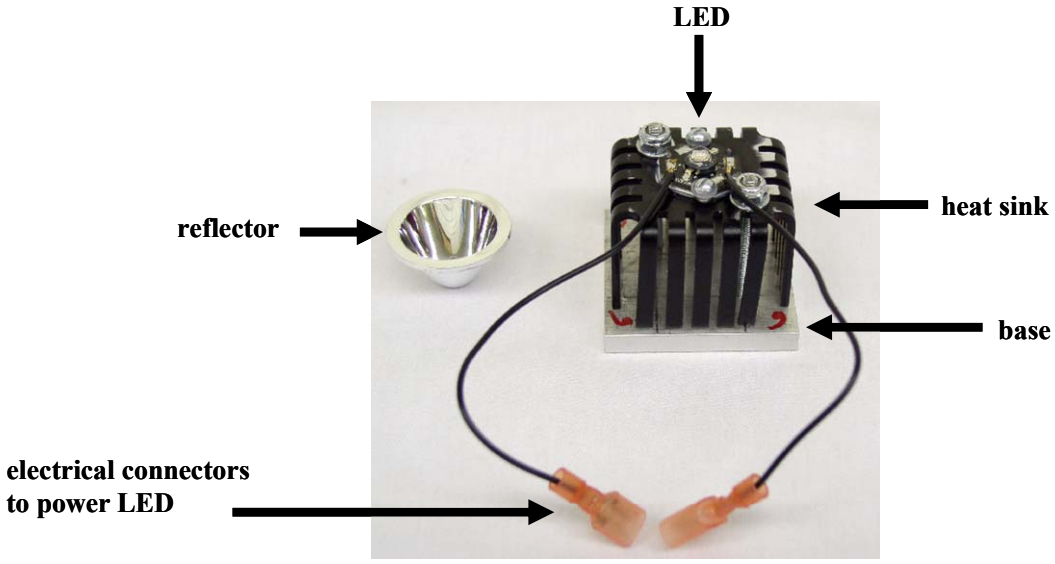

Figure 2.9 A. Truncated circuit diagram for the third generation LED array. The diagram shown only contains two of the eight LED wire runs. In the diagram R1 and R3 refer to the 7.5 ohm resistors, R2 and R4 refer to the 10 ohm resistors, and R5 and R6 refer to the 5 ohm resistors. RH1 and RH2 refer to the 25 ohm rheostats which have been assigned a value of 50% however, they are adjusted as needed in the array. S1 and S2 are switches, D1 and D2 are LEDs, and Vs1 refers to the 13.8 V DC power supply. **B.** Interchangeable LED unit consisting of an LED that is mounted onto a heat sink, which is rigidly attached to the aluminum base. The LED units utilize disconnects. The reflector shown to the left of the LED unit is attached around the LED and used to focus light on the sample.

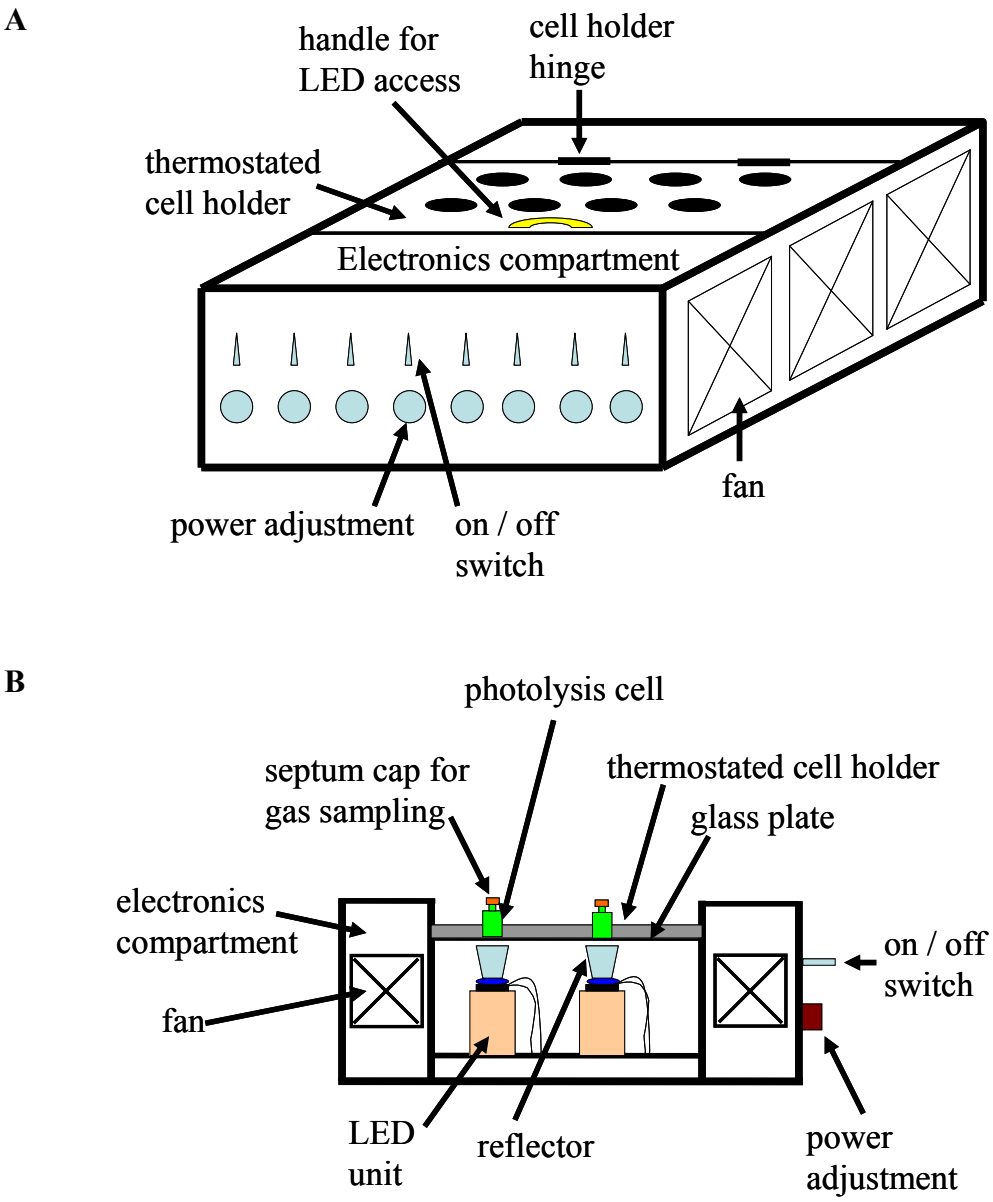

Figure 2.10 Schematics of the third generation photolysis system displaying **A.** front view and **B.** side cut out.[a]

[a]The array is thermostated and accommodates up to eight samples for photolysis. The LEDs can be controlled via toggle switches. Power to each LED is controlled by rheostats that are accessed through knobs on the instrument panel. The array irradiates samples from beneath and allows for modulation of LEDs.

Luxeon V 5 W LEDs and Prolight 5 W LEDs have a maximum forward current rating of 700 mA of DC current. Longer wavelength LEDs are operated at 5 V DC while the

shorter wavelength LEDs are operated at 7 V DC. This third generation array has allowed for this variance by incorporating different resistors for the two different inputs of the spdt switch. The third generation array has the ability to control the power to each LED within the operating range. In this way the output of each LED can be modulated to match the output of any other LED. This control was made possible by the circuit design. In the design the LEDs are in series with their respective resistors. As shown in Figure 2.9A, each series-parallel wire run contains one resistor to limit the power to the LED and another set of resistors, which are in parallel and are composed of a rheostat and a resistor. The first resistor is 7.5 ohms for the short wavelength (7 V) LEDs or 10 ohms for the long wavelength (5 V) LEDs. This second set of resistors is composed of a 5 ohm resistor in parallel with a 25 ohm rheostat, and acts as a dimmer to vary the power to the LED within the operating range. All resistors have a tolerance of ± 1 %.

2.5 Third Generation Array Calibration

The third generation array was calibrated by adjusting the operating current to 0.698 mA with a digital multi-meter, and subsequently measuring the power output with the calorimeter, Figure 2.11. This procedure was done with all LEDs. For each wavelength of LED the average calorimetric power output was determined and used as the calibration value for all subsequent experiments.

A

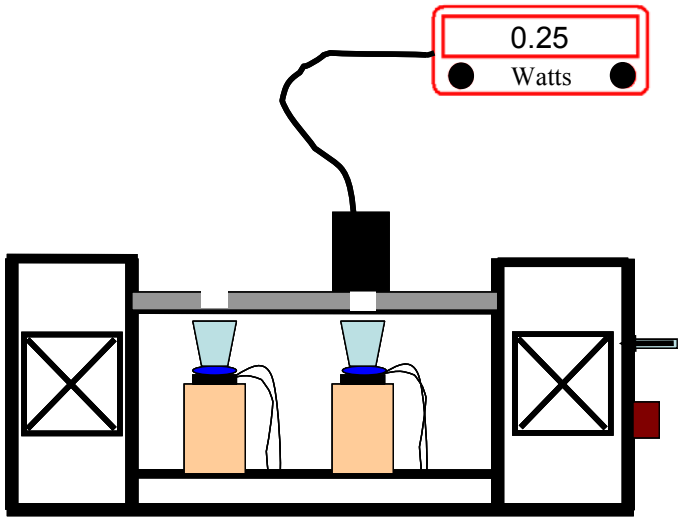

B

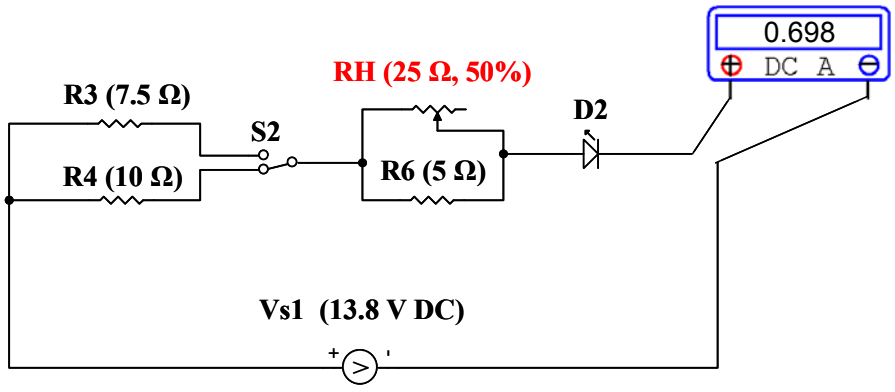

Figure 2.11 A. Side cut-out of the third generation LED array showing position of calorimeter for array calibration. **B.** Truncated circuit diagram for the third generation LED array. The diagram shown only contains one of the eight LED wire runs. The diagram shows how a digital multi-meter can be inserted in series with the circuit for accurate determination of the current for an LED.

2.6 Constant Current Drivers

Constant current drivers were also investigated as an alternate power source for the LEDs, specifically in the 3rd generation LED array. Two Xitanium (Advance Transformer Company) LED drivers were investigated. Figure 2.12A shows the circuit diagram of four LEDs in the 3rd generation LED array, powered by a constant current driver. The driver provides 17 W 700 mA output, and powers the LEDs in series. Figure 2.12B displays a circuit diagram of eight LEDs in the 3rd generation LED array powered by a 25 W 1050 mA constant current driver. Power is supplied to two parallel wire runs; with four LEDs in each wire run. Both drivers required a 120 V AC input, which was obtained from wall power outlets. In both cases the 3rd generation LED array housing and LED units were used for evaluation purposes. Drivers were evaluated by measuring the power output of the LEDs in the 3rd generation array. The array was assembled as usual with the exception that the LEDs were wired to the Xitanium driver instead of the 13.8 V DC circuit. The constant current drivers were evaluated by calorimetry. The power output of the LEDs were measured as the number of LEDs in the circuit was varied from a single LED to the maximum load of four or eight LEDs.

A

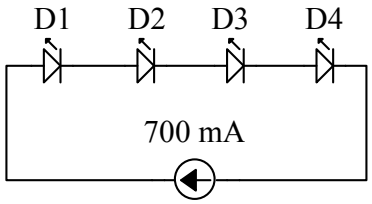

B

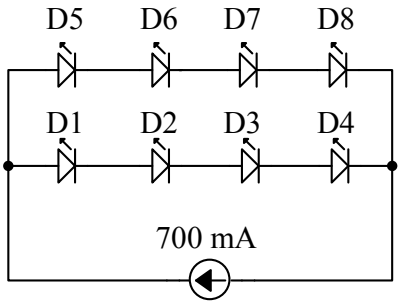

Figure 2.12 A. Circuit diagram of four LEDs in the 3rd generation LED array powered in series by a constant current driver. The driver is an Advance Transformer Corp. Xitanium driver with a 17 W 700 mA output. **B.** Circuit diagram of eight LEDs in the 3rd generation LED array powered in two parallel series by a constant current driver. The driver is an Advance Transformer Corp. Xitanium driver with a 25 W 1050 mA output.

2.7 Photocatalysis with a Xe Arc Lamp

A 1000 W Xe arc lamp was used as a standard comparison for the LED arrays, Figure 2.13. The photonic output was filtered using a NIR water filter in conjunction with a 460 ± 5 nm full width at half max (FWHM) interference filter. The light was collimated using a focusing lens and directed onto the sample. The sample cell is a cylindrical cell situated on a thermostated cylindrical cell holder. The cell holder, filter, and collimating lens were all oriented along an optical rail. Figure 2.14A shows the spectral irradiance data for an Oriel research grade 1000 W Xe arc lamp.

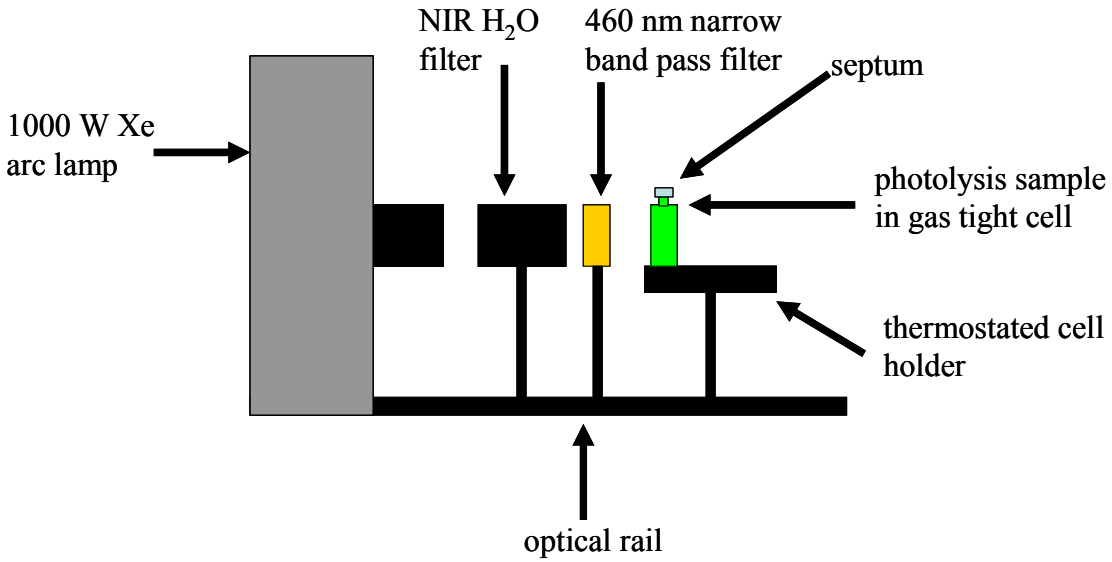

Figure 2.13 Xe arc lamp photolysis system for the photochemical production of H_2 from water using supramolecular catalysts.

Figure 2.14B shows the percent transmittance of the 460 ± 5 nm FWHM interference filter used in the present study.

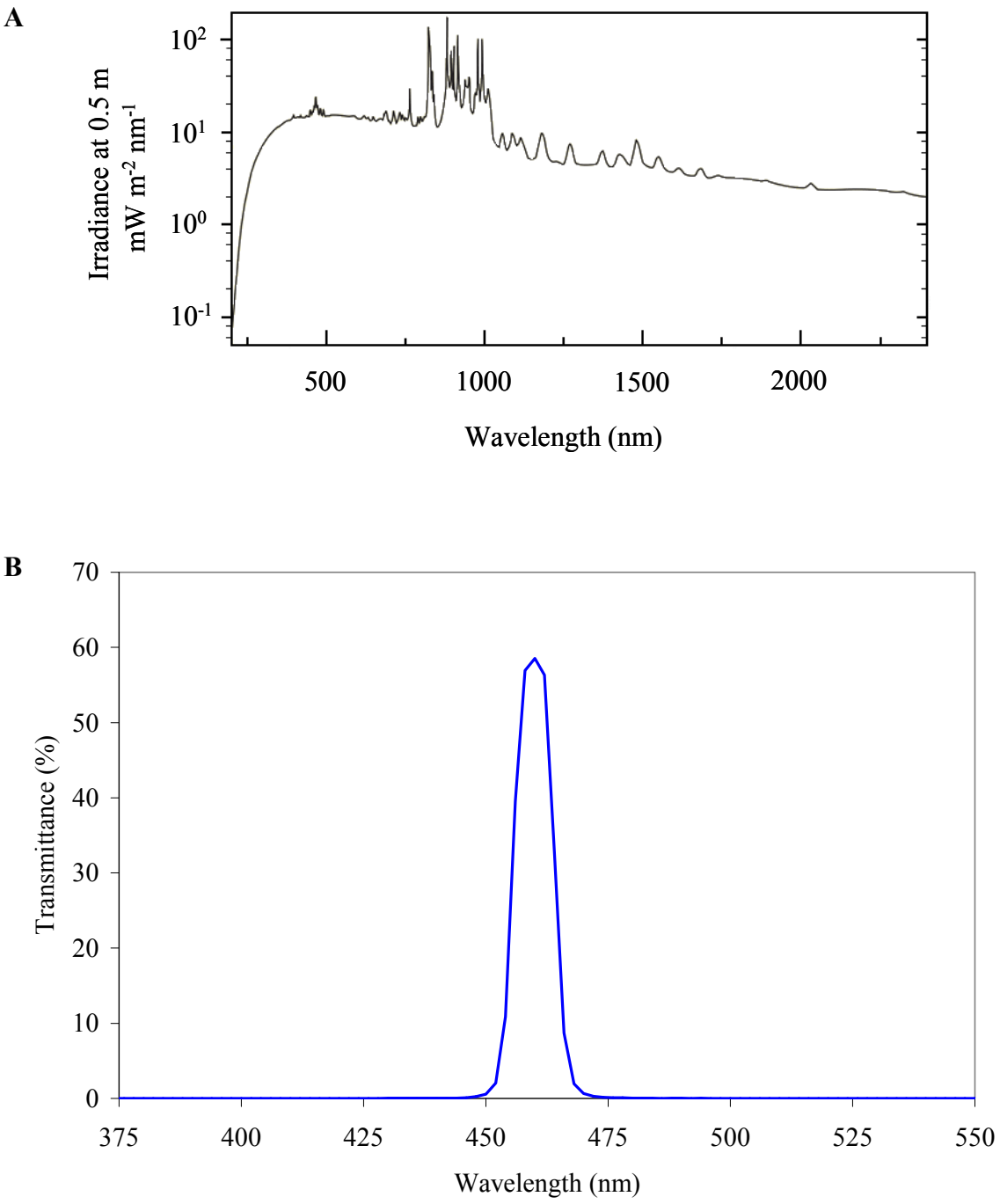

Figure 2.14 A. Spectral irradiance data of Oriel 1000 W Xe arc lamp. **B.** Percent transmittance spectrum for 460 nm interference filter used with 1000 W Xe arc lamp for wavelength selection. Filter limits spectral output to 460 nm, 10 nm FWHM.

2.8 Photocatalytic Hydrogen Production

2.8.1 Experimental Design

Photocatalytic hydrogen production experiments were carried out by preparing a 7:1 acetonitrile/water solution containing $[\{(bpy)_2Ru(dpp)\}_2RhCl_2](PF_6)_5$ (80.0 μM), dimethylaniline (DMA) (0.890 M) as an electron donor, and acidified water (pH 2, HCl). Metal complex solutions were prepared using Burdick and Jackson UV-grade acetonitrile. Catalyst concentration was adjusted to 104 μM using the published extinction coefficient (ε = 20100 M^{-1} cm^{-1}) that corresponds to the Ru(dπ)→dpp(π*) MLCT transition occurring at 514 nm.[35] Into the custom built photolysis cells 22 (O.D.) × 30 mm, 5.5 mL total volume, was added 3.50 mL of the prepared catalyst solution. A 0.500 mL aliquot of acidified water (pH 2, HCl) was added. The cell was septum capped and deoxygenated with argon for ~10 min. DMA, which had been deoxygenated with argon, was then syringed into the septum capped cells in the amount of 0.500 mL. The DMA was added under an argon flow, and the final solution was deoxygenated for ~30 s. The final solution was photolyzed using LED arrays for a specified time usually 1-4 hrs. The hydrogen was quantified by sampling the headspace of the photolysis cell. Hamilton gas tight syringes were used to syringe out 50 μL from the ~1mL headspace. The gaseous sample was then injected into a GOW-MAC series 580 gas chromatograph equipped with a Hewlett Packard model 1243A integrator. Separations were performed on a ¼ (O.D.) column packed with 5 Å molecular sieve solid support. Hydrogen was detected with a thermal conductivity detector under the following conditions: injection

port 150 °C, column oven 165 °C, detector 180 °C, detector current 150 mA, Ultra-high purity argon was used as the carrier gas, and the detector filament was tungsten-rhenium.

2.8.2 Analysis

The total amount of hydrogen produced was calculated by taking into consideration the amount of H_2 in the headspace as well as the H_2 in the photolysis solution. The amount of hydrogen in the headspace was determined using a calibration curve to calculate the amount of H_2 in the headspace sample analyzed by gas chromatography, GC, and then accounting for the total volume in the headspace. The calculation is shown in equation 2.17 where $H_{2\ H.S.}$ is the amount of hydrogen in the headspace, $H_{2\ cal}$ is the amount of hydrogen in the analyzed injection as determined from the calibration curve, $H.S._{vol}$ is the volume of the headspace, and Inj_{vol} is the volume of hydrogen analyzed by GC.

$$H_{2\ H.S.} = \frac{(H_{2\ cal})(H.S._{vol})}{Inj_{vol}} \tag{2.17}$$

A representative H_2 calibration is shown in the appendix. The calibration was performed as follows. Four 125 mL Erlenmeyer flasks were filled with water and septum capped. A needle was inserted into the septum as the flask was capped to allow for displacement. The volume of each flask was then determined by measuring the mass of the water in the flask and using the density of water to calculate the volume of the flask. The flasks were deoxygenated with argon for 20 min each, and ~ 1.4 mL of hydrogen (enough to make

the flask 1 % H_2) was then syringed into the flasks using a Hamilton Gas Tight syringe. Sample injections were made from each flask ranging from 20-100 μL.

The amount of hydrogen in the photolysis solution was calculated by determining the saturation mole fraction of H_2 in acetonitrile, χ_{sat}, at room temperature and under 1 atm of H_2. The saturation limit of H_2 in acetonitrile was determined as follows. A 25 mL aliquot of Burdick and Jackson UV-grade acetonitrile was septum capped in a 50 mL Erlenmeyer flask. The solution was then bubbled with H_2 for ~30 min, after which, an aliquot (10 μL) of the H_2 saturated acetonitrile was syringed out using a Hamilton Gas Tight syringe and injected into the GC for H_2 analysis. Equation 2.18 shows the calculation of the saturated mole fraction of H_2 in acetonitrile, χ_{sat}, where n_{H2} refers to the number of moles of hydrogen in the acetonitrile injection, n_{total} refers to total moles in the injection (the moles of acetonitrile can be used as a very good approximation), V_{H2} is the volume of hydrogen in the acetonitrile injection, MW_{CH3CN} is the molecular weight of acetonitrile, V_{CH3CN} is the volume of acetonitrile analyzed, D_{CH3CN} is the density of acetonitrile, and SMV is the molar volume of an ideal gas at 1 atm and 298.15 K. The calculation is shown in equation 2.19.

$$\chi_{sat} = \frac{n_{H_2}}{n_{total}} = \frac{(V_{H_2})(MW_{CH_3CN})}{(V_{CH_3CN})(D_{CH_3CN})(SMV)} \tag{2.18}$$

$$\chi_{sat} = \frac{(7.8\times10^{-7}\,L)(41.06\,g\cdot mol^{-1})}{(0.01mL)(0.7857\,g\cdot mL^{-1})(24.788\,L\cdot mol^{-1})} = 1.61\times10^{-4} \tag{2.19}$$

The calculated mole fraction agreed well with the literature value of 1.78×10^{-4}.[36]

The amount of hydrogen in the solution can then be calculated according to Henry's Law, equation 2.20. P_{H2} is the partial pressure of hydrogen in the photolysis cell headspace, P_{sat} is the partial pressure of hydrogen in the hydrogen saturation experiment, K_H is Henry's law constant, χ_{H2} is the mole fraction of hydrogen in the photolysis cell solution, and χsat is the mole fraction of hydrogen in the hydrogen saturation experiment. This can be rearranged to solve for the mole fraction of hydrogen in the photolysis solution taking χ_{sat} = 1 atm H_2, equation 2.21. The amount of hydrogen in the photolysis solution is then determined according to equation 2.22 where V_{sol} is the volume of the photolysis solution, and n_{H2} is the amount of moles of hydrogen in the solution.

$$\frac{P_{H_2}}{P_{sat}} = \frac{(K_H)(\chi_{H_2})}{(K_H)(\chi_{sat})} \tag{2.20}$$

$$\chi_{H_2} = \frac{(P_{H_2})(\chi_{sat})}{(P_{sat})} = (P_{H_2})(\chi_{sat}) \tag{2.21}$$

$$n_{H_2} = (V_{sol})(\chi_{H_2}) \tag{2.22}$$

The total volume of hydrogen produced in a photolysis experiment is then the sum of the hydrogen found in the headspace as well as the hydrogen found in the solution. Typically the contribution of hydrogen in solution amounts to ~20 % of the total volume of hydrogen. The typical error in these experiments is ± 4-7 %

2.9 Statistical Evaluation

2.9.1 General Statistics

A series of potassium tris(oxalato)ferrate(III) actinometry experiments and radiant energy measurements were performed using a 1000 W Xe arc lamp with a 460 ± 5 (FWHM) nm narrow band pass filter and with each generation of the LED arrays. The experiments were done to compare the standard Xe arc lamp method with the LED method of photolysis. Statistical treatments were used to evaluate both the Xe arc lamp and the LED array photolysis systems. The data were evaluated using general statistics by determining the coefficient of variance (CV) which is defined as the ratio of the standard deviation to the mean, and by confidence integrals (CL) of 95% probability, thus, providing limits around the mean with which the true population may be found.[37]

2.9.2 Hypothesis Testing

In hypothesis testing there are two hypotheses, the first is termed the null hypothesis and is always the simplest hypothesis. The null hypothesis states that there is no difference between series of data sets, or that all differences are due to random error. The second hypothesis is that there is a difference between series. The user defined significance of the calculation is represented by α, and is a type 1 error. A type 1 error is finding a true hypothesis false. When α is assigned a value of 0.05 there is a 5% probability that the null hypothesis, which is the default hypothesis, will be incorrectly rejected. Measurements can be expressed as linear combination of terms such as $y_{ij} = \mu +$

$\tau_i + \varepsilon_{ij,}$ where i represents a particular series or treatment evaluated, j represents a replicate measurement taken within a series, y_{ij} represents an individual measurement, μ is the data mean, τ_i is the series or treatment effect, and ε_{ij} represents random error. The null effect is true when τ_i is zero and sample variance is due to random error.[38,39]

Analysis of variance (ANOVA) is a statistical method of hypothesis testing which compares the means from different series or treatments to determine the proportion of variance that is due to the different series as compared to the variance as a result of random error within a user defined level of significance. ANOVA calculations are broken into "sum of squares" that determine the variance due to random error and that due to a difference in series or treatments. The "sum of squares" is expressed as $SS_T = SS_L + SS_E$ where SS_T is the total sum of squares, SS_L is the sum of squares due to the series or treatments and SS_E is the sum of squares due to random error.[38,39]

$$SS_T = \sum_{i=1}^{x}\sum_{j=1}^{n_i}(y_{ij})^2 - \frac{\left(\sum_{i=1}^{x}(y_i)\right)^2}{N} \tag{2.23}$$

$$SS_L = \sum_{i=1}^{x}\frac{(y_i)^2}{n_i} - \frac{\left(\sum_{i=1}^{x}(y_i)\right)^2}{N} \tag{2.24}$$

In equations 2.23 and 2.24, x represents the total number of i series, n_i the total number of replicate measurements in series i, y_i represents the sum of measurements within series i, and N is the total number of measurements made. SS_E is determined by subtraction.

Mean squares, which are the sum of squares relative to their individual degrees of freedom, are then calculated.

$$MS_L = \frac{SS_L}{df_L} \tag{25}$$

$$MS_E = \frac{SS_E}{df_E} \tag{26}$$

In equations 2.25 and 2.26, MS_L represents the mean squares of the series or treatments, MS_E is the mean squares of random error, df_L and df_E represent the degrees of freedom for the series and random error sum of squares calculations respectively. df_L and df_E are defined as (x – 1) and (N – x) respectively. The F (Fisher) ratio is then calculated where F is the ratio of MS_L to MS_E. If $F \geq F_{crit}$ (F_{crit} is calculated from α, x-1, N-x) then the null hypothesis is rejected and it is concluded that there is a statistically significant difference between the series or treatments within the user defined probability, and that all variability is not due to random error alone.[38,39] In all statistical evaluations performed α was assigned a value of 0.05.

2.9.3 Data Distribution

The statistical methods used to evaluate the experimental data require that the data be normally distributed. A convenient method of evaluating the distribution of data is by Rankit plots. The Rankit plots were performed in Excel as follows. The data are arranged in ascending order, each datum is given a cumulative frequency, CF, a value

Table 2.3 The cumulative frequency for a series of 6 data.

Data	Cumulative frequency
0.048	1
0.050	3
0.050	3
0.051	5
0.051	5
0.052	6

assigned based on how many data have an equal or lesser value than the present datum. An example is shown above in Table 2.3. (the cumulative frequency is assigned in descending order from the first (smallest datum) to the last (largest datum), the cumulative frequency was normalized according to equation 2.27 where NCF is the normalized cumulative frequency, CF is the cumulative frequency and n is the total number of data being evaluated.[38]

$$NCF = \frac{\mathrm{CF}}{(\mathrm{n}+1)} \tag{2.27}$$

The z values were calculated in Excel using the =NORMSINV(NCF) function where NCF is the cell containing the normalized cumulative frequency. NORMSINV returns a value, z, such that the NCF is equal to the probability density function, pdf, (Gaussian distribution function) integrated from minus infinity to z. The pdf is generated by Excel with data, x, such that the population mean, u, is zero and the population standard

deviation, σ, is 1. Equation 2.28 shows the function NORMSINV. Excel was used due to the nontrivial nature of the calculation.

$$z, \textit{such that } NCF = \int_{-\infty}^{z} \frac{e^{\left[-\frac{(x-u)^2}{2\sigma^2}\right]} \cdot dx}{\sigma\sqrt{2\pi}} = \int_{-\infty}^{z} \frac{e^{\left(-\frac{x^2}{2}\right)} \cdot dx}{\sqrt{2\pi}} \qquad (2.28)$$

The Rankit method plots the data (x-axis) against the value, z, of the normal probability function associated with the cumulative frequency of the data. If the data are normally distributed the Rankit plot should approximate a straight line. The Rankit plots are included in the Appendix as supporting information.

Suspect data were tested to determine outliers using the Grubbs test shown in equation 2.29 where G is the Grubbs number, $X_{suspect}$ is the datum in question, M is the data mean, and s is the sample standard deviation of the data set.

$$G = \frac{\left|X_{suspect} - M\right|}{s} \qquad (2.29)$$

The G value calculated is then compared with a tabulated $G_{critical}$ value at the percent confidence required. If $G > G_{critical}$ then the suspect point is rejected.[38] No outliers were detected at 95 % confidence. Included in the Appendix are plots of the data for each experiment with highlighted an $X_{suspect}$ value such that $G = G_{critical}$. These suspect values represent the maximum and minimum values prior to the data being an outlier.

Chapter 3. RESULTS AND DISCUSSION

3.1 Synthesis

Supramolecular complexes can be thought of as multifunctional complexes composed of multiple components contributing functionality to the whole. The catalyst used in hydrogen production experiments is the Ru, Rh, Ru trimetallic complex $[\{(bpy)_2Ru(dpp)\}_2RhCl_2](PF_6)_5$. The supramolecular complex is composed of two Ru light absorbers, LA, bound to a reactive Rh center, EC, through the bridging ligand, BL. The complex then follows a LA-BL-EC-BL-LA structural motif, Figure 3.1. The synthesis of this

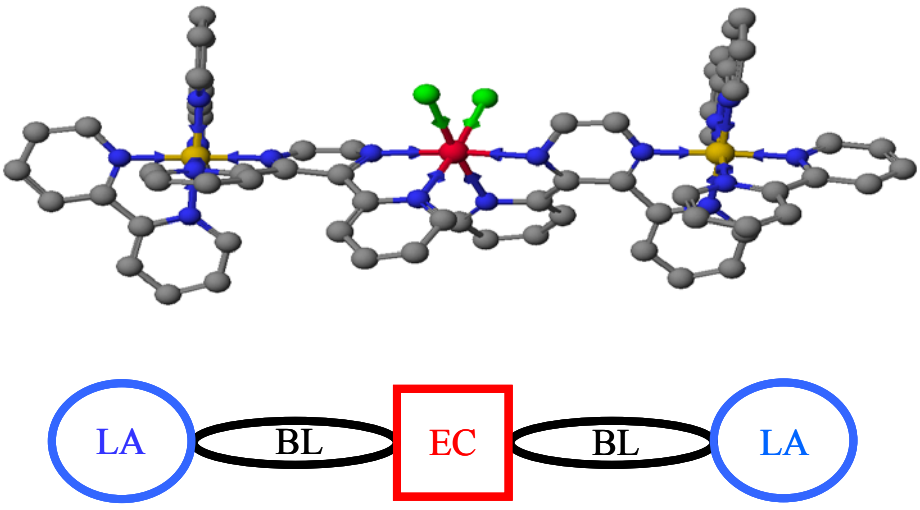

Figure 3.1 Supramolecular complex $[\{(bpy)_2Ru(dpp)\}_2RhCl_2](PF_6)_5$ is composed of two Ru light absorbers, LA, bound to a reactive Rh center, EC, through the bridging ligand, BL (bpy = 2,2'-bipyridine and dpp = 2,3-bis(2-pyridyl)pyrazine).

complex follows a building block method, constructing and combining the individual components, Figure 3.2. This structural motif lends itself to perturbations as the individual components can be modulated without negating the overall synthetic route.

The syntheses were all performed according to literature procedures.[32] The reaction conditions are mild and all syntheses resulted in moderate yields. The $[Ru(bpy)_2Cl_2]$ light absorbing unit can be purchased commercially, however, as the purification of impurities such as $[Ru(bpy)_3]Cl_2$ is required, this complex was synthesized. $[Ru(bpy)_2Cl_2]$ was synthesized by refluxing 1 equivalent of $RuCl_3{\cdot}3H_2O$ with two equivalents of bpy to yield $[Ru(bpy)_2Cl_2]$. The product was isolated from the mother liquor with acetone, and purified by washing with copious amounts of water.

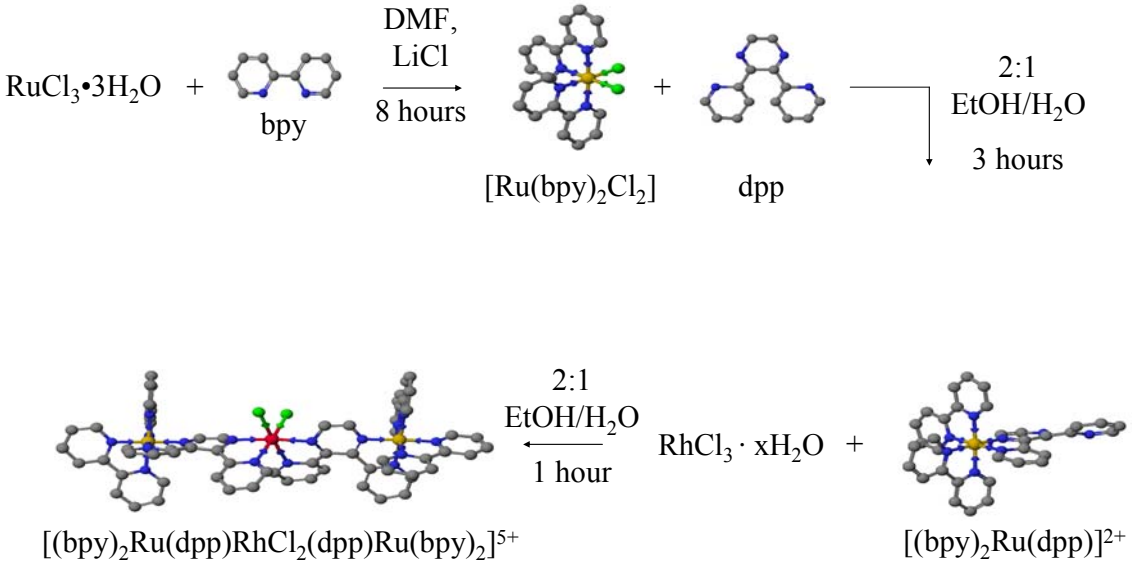

Figure 3.2 Building block synthesis for the supramolecular complex $[\{(bpy)_2Ru(dpp)\}_2RhCl_2](PF_6)_5$ (bpy = 2,2'-bipyridine and dpp = 2,3-bis(2-pyridyl)pyrazine).[32]

According to the building block method, after the synthesis of the $[Ru(bpy)_2Cl_2]$ light absorbing unit the bridging ligand, dpp, is attached by heating at reflux in 2:1 ethanol/water. The major impurity formed is the bimetallic species $[\{(bpy)_2Ru\}_2(dpp)](PF_6)_4$, which is removed by column chromatography. The final step in this method is the combination of the synthesized Ru monometallic complex $[(bpy)_2Ru(dpp)](PF_6)_2$ with $RhCl_3 \cdot 3H_2O$ by heating at reflux in 2:1 ethanol/water. This complex is purified by recrystallization from hot ethanol.

3.2 Electrochemistry

All complexes were characterized by comparison of electronic absorption spectroscopy and electrochemical data with published values.[19,35,40] As all the complexes synthesized are known the discussion will focus on the supramolecular complex $[\{(bpy)_2Ru(dpp)\}_2RhCl_2](PF_6)_5$ investigated in photochemical hydrogen production experiments. The electrochemical behavior of this complex is characterized by overlapping ruthenium oxidations, irreversible rhodium reductions, and reversible ligand reductions. A typical cyclic voltammogram for the trimetallic complex is given in Figure 3.3. This complex displays a Ru ($d\pi$) highest occupied molecular orbital (HOMO). The lowest unoccupied molecular orbital (LUMO) is Rh ($d\sigma^*$). Table 3.1 presents the electrochemical properties of $[\{(bpy)_2Ru(dpp)\}_2RhCl_2](PF_6)_5$, which are all in agreement with literature

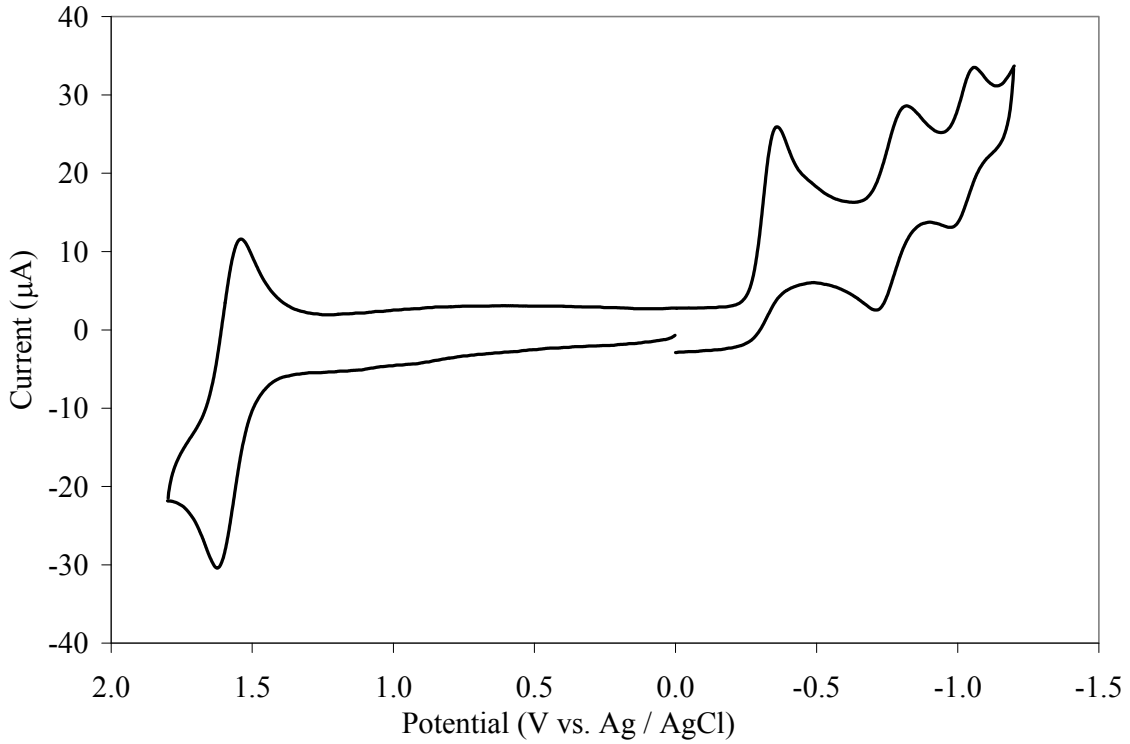

Figure 3.3 Cyclic voltammogram of the trimetallic complex $[\{(bpy)_2Ru(dpp)\}_2RhCl_2](PF_6)_5$ in 0.1 M Bu_4NPF_6 in CH_3CN at room temperature with a scan rate of 100 mV/s (bpy = 2,2'-bipyridine and dpp = 2,3-bis(2-pyridyl)pyrazine). Potentials recorded vs. Ag / AgCl reference electrode (0.29 V vs. NHE).

values.[35] A reversible redox couple occurs at 1.60 V vs. Ag / AgCl corresponding to the two overlapping $Ru^{II/III}$ oxidations. The Ru redox potential observed is consistent with that of a $(bpy)_2Ru(\mu\text{-dpp})$ coordination environment.[41] It can be seen that there is little communication between the Ru metals as only one redox couple is observed. In general if there is electronic communication between metal centers, then a splitting of the Ru oxidations would be evident. This uncoupled environment allows the two Ru LAs to function independently. The first redox event observed on a cathodic scan occurs at E_p^c = -0.39 V and is assigned as the $Rh^{III\,/\,II\,/\,I}$ irreversible reduction.

Table 3.1 Electrochemical properties of $[\{(bpy)_2Ru(dpp)\}_2RhCl_2](PF_6)_5$.

Assignment	$E_{1/2}$ in V[a] (ΔEp in mV)
2 $Ru^{III/II}$	1.60 (80)
$Rh^{III/II/I}$	E_p^c = -0.39
dpp, dpp / dpp, dpp^-	-0.79 (85)
dpp, dpp / dpp^-, dpp^-	-1.02 (110)

[a]Potentials reported versus the Ag / AgCl reference electrode in 0.1 M Bu_4NPF_6 room temperature CH_3CN (0.29 V vs. NHE).

Conversion from the 18 e^- d^6 psuedo octahedral Rh^{3+} complex to the 16 e^- d^8 Rh^{1+} complex is accompanied by transition to a square planar geometry with loss of the two chlorides consistent with the electrochemical behavior of $[Rh(bpy)_2Cl_2]$.[19,42] Continuing to scan cathodically two reversible redox couples are observed and attributed to the equivalent dpp bridging ligands. The first of the two reductions dpp, dpp / dpp, dpp^- occurs at -0.79 V and the second dpp reduction dpp, dpp^- / dpp^-, dpp^- occurs at -1.02 V. The $dpp^{0/-}$ redox couples observed are consistent with that of a $(bpy)_2Ru(\mu\text{-dpp})$ coordination environment.[41]

3.3 Electronic Absorption Spectroscopy

The electronic absorption spectrum of $[\{(bpy)_2Ru(dpp)\}_2RhCl_2](PF_6)_5$ in room temperature acetonitrile is presented in Figure 3.4. The absorption spectrum is characterized by intraligand $\pi \rightarrow \pi^*$ and $n \rightarrow \pi^*$ transitions in the UV region. The spectrum is composed of many overlapping transitions, of note are the bpy ($\pi \rightarrow \pi^*$)

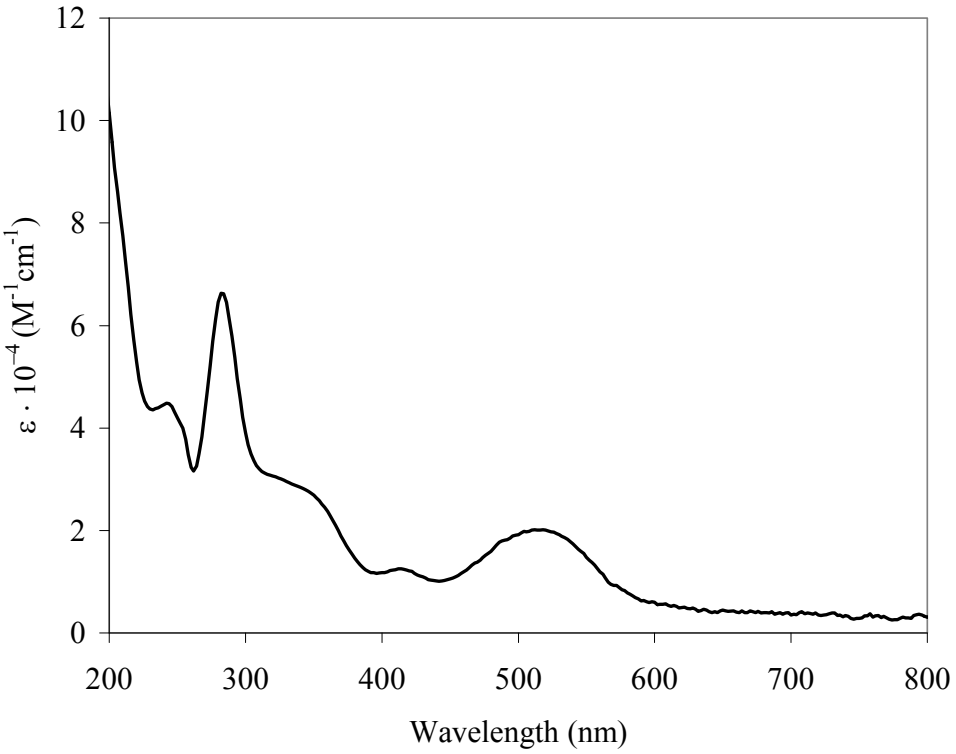

Figure 3.4 Electronic absorption spectrum of $[\{(bpy)_2Ru(dpp)\}_2RhCl_2](PF_6)_5$ in CH_3CN at room temperature. (bpy = 2,2'-bipyridine and dpp = 2,3-bis(2-pyridyl)pyrazine).

transitions at 242 nm and 284 nm. The shoulder occurring at 344 nm is assigned to the ($\pi \rightarrow \pi^*$) transition of the bridging ligand dpp. The visible region is characterized by two metal-to-ligand charge transfer transitions (MLCT). The higher energy MLCT occurs at 414 nm and is assigned to the Ru ($d\pi$)→bpy (π^*) CT transition. The lower energy MLCT occurring at 514 nm is assigned to the Ru ($d\pi$)→dpp (π^*) CT transition. The electronic absorption spectrum observed correlates very well with similar literature examples such as $[\{(bpy)_2Ru\}_2(dpp)](PF_6)_2$.[9] Table 3.2 presents the assigned transitions for the

Table 3.2 Electronic absorption spectroscopy of $[\{(bpy)_2Ru(dpp)\}_2RhCl_2](PF_6)_5$ in CH_3CN at room temperature.

$Absorbance_{max}$ (nm)	$\varepsilon \times 10^{-4}$ (M^{-1} cm^{-1})	Assignment
242	6.53	bpy ($\pi \rightarrow \pi^*$)
284	9.64	bpy ($\pi \rightarrow \pi^*$)
344(sh)	2.87	dpp ($\pi \rightarrow \pi^*$)
414	1.74	Ru ($d\pi$)$\rightarrow$bpy (π^*) MLCT
514	2.01	Ru ($d\pi$)$\rightarrow$dpp (π^*) MLCT

trimetallic complex as well as the literature values of their respective extinction coefficients.[19] The properties of this complex that make it applicable as a solar hydrogen production catalyst are due to the nature of the electronic transitions, specifically charge transfer to the BL, and the electronic coupling of the two Ru LAs to the central Rh core through covalent linkages. It is the combination of ground state electronic properties, specifically of the two light absorbing Ru HOMOs and a central Rh LUMO, combined with the excited state properties such as a lowest-lying Ru ($d\pi$)$\rightarrow$dpp (π^*) MLCT that have sparked interest in this complex as a molecular device.

3.4 Molecular Devices

$[\{(bpy)_2Ru(dpp)\}_2RhCl_2](PF_6)_5$ is by design a supramolecular device for photoinitiated electron collection. The Rh core can collect multiple electrons or reducing equivalents when photolyzed in the presence on an electron donor such as dimethylaniline (DMA).[43]

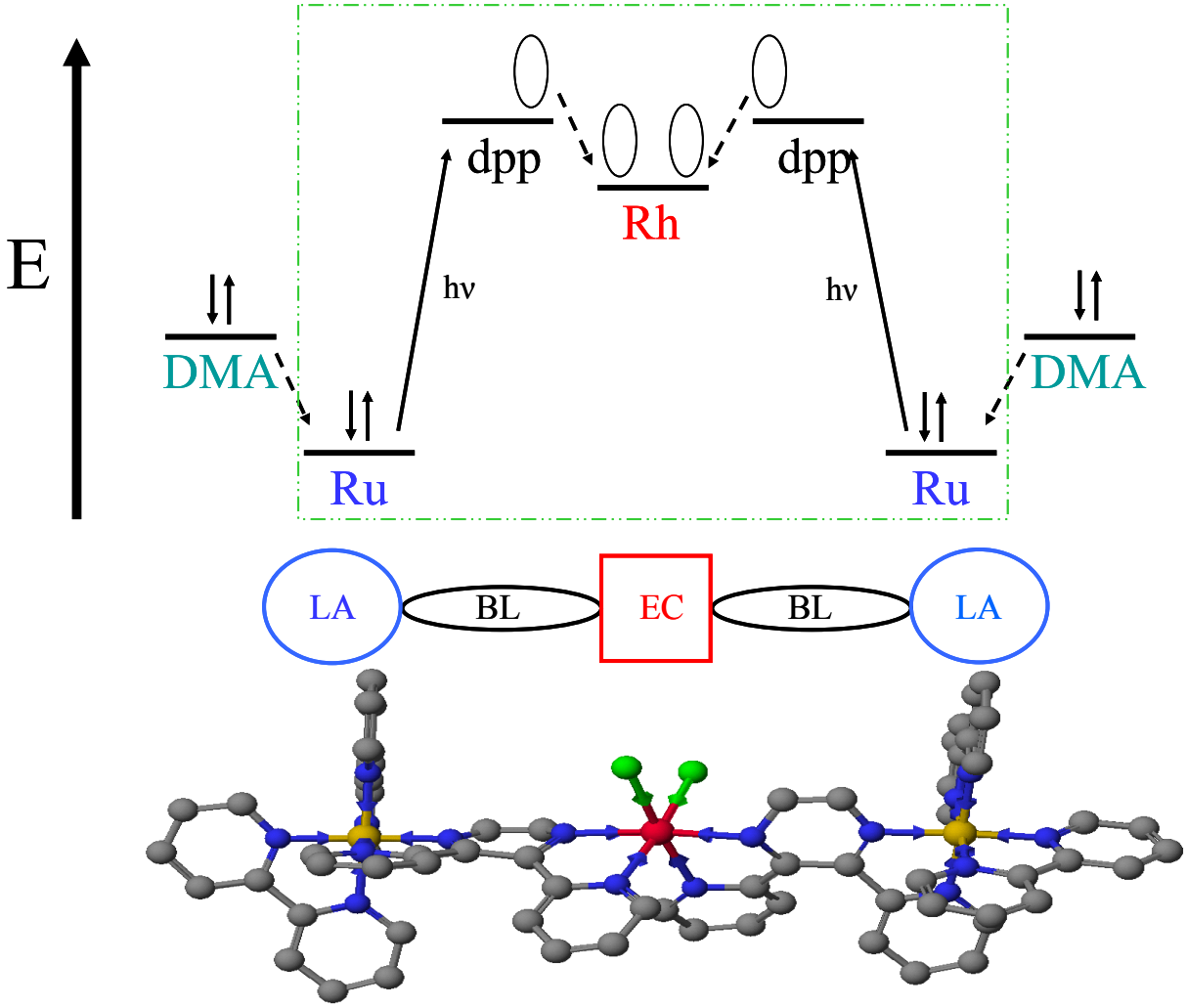

Figure 3.5 Schematic representation of $[\{(bpy)_2Ru(dpp)\}_2RhCl_2](PF_6)_5$ as a supramolecular device for photoinitiated electron collection. Electron collection occurs upon photolysis in the presence an electron donor such as dimethylaniline (DMA). Orbital energy diagram shows the device functioning (ED = electron donor, LA = light absorber, BL = bridging ligand, EC = electron collector).

Spectroelectrochemical studies have shown that the two electron reduced complex displays an electronic absorption spectrum identical to the photoreduced complex.[43] Photoinitiated electron collection is shown schematically in Figure 3.5.[44] As can be seen

the complex is symmetrical with respect to Ru-Rh-Ru, and electron collection can occur by two identical LA-BL-EC pathways. Photoinitiated electron collection can be broken down into two mechanisms, where each mechanism can take place through both identical LA-BL-EC pathways. The first mechanism consists of three steps. First, the Ru light absorber, LA, absorbs a photon with concurrent electron transfer to the bridging ligand (MLCT). Second, the electron donor, ED, donates an electron to the Ru LA preventing relaxation of the excited Ru by filling the Ru ($d\pi$) vacancy created by absorption of light. Third, the promoted electron then propagates to the lower energy orbital on the Rh center, EC. In the second mechanism the Ru light absorber, LA, absorbs a photon with concurrent e^- transfer to the Rh center, metal to metal charge transfer (MMCT). The electron donor, ED, then donates an electron to the Ru LA filling the Ru ($d\pi$) vacancy created by electron transfer. The total process by either mechanism produces two singly oxidized electron donors and a doubly reduced electron collecting Rh core. The nature of the light absorbing metal as well as bridging and terminal ligands all affect device functioning.

3.5 Hydrogen Production Catalysis

Supramolecular complexes capable of multi-electron chemistry have excited attention in recent literature.[45] The activation of small molecules requires multiple electrons; as such complexes capable of transferring multiple electrons are interesting targets for investigation. $[\{(bpy)_2Ru(dpp)\}_2RhCl_2](PF_6)_5$ is a molecular device for photoelectron collection, and the Rh core has been shown to be electrocatalytically active

towards CO_2 reduction.[46] Initial investigations were made as to the complex functioning as a catalyst for hydrogen production from water. Initial experiments met with success.[47] The system consisted of the $[\{(bpy)_2Ru(dpp)\}_2RhCl_2](PF_6)_5$ and DMA combined in 7:1 acetonitrile/H_2O and photolyzed for 2 hr with a 1000 W Xe arc lamp. Many perturbations are necessary to understand and optimize the production of hydrogen from a supramolecular complex. These include modulating the supramolecular complex, the electron donor, the water source, the pH, the solvent, the wavelengths and intensity of the light source, etc. As such, an alternate high-throughput method of investigation was needed to perform the necessary perturbations in rapid and reliable manner.

3.6 Light Emitting Diodes

LEDs have many advantages as a photolysis source being nearly monochromatic, modular, and reproducible with long lifetimes and low power consumption. For these reasons a rigorous investigation of LEDs as a photolysis source compared to traditional Xe arc lamps was undertaken. Table 3.3 presents a comparison of a research grade Oriel 1000 W Xe arc lamp versus the LEDs used in the present research. Two factors of paramount importance with respect to photochemical research are wavelength control and light source stability. The Xe arc lamp and LEDs both display very high precision. However, when comparing multiple lamps and multiple LEDs the precision of both systems drops to ± 10 % for LEDs and slightly lower for arc lamps. Wavelength selection is easily and reliably accomplish in arc lamp systems by filters. LEDs systems accomplish wavelength selection by the choice of LED. Luxeon LEDs are available over

Table 3.3 Comparison of Luxeon 5 W LEDs with a standard research grade 1000 W Xe arc lamp.

	1000 W Xe arc lamp	Luxeon 5 W LED
Spectral output	Continuous 200-2500 nm	Continuous 425-775 nm[a]
Wavelength selection	Filters	LED selection (20 nm FWHM)
Power consumption	1000 W	5 W per LED
Lifetime	1000 hr per bulb ($630 per bulb)	100,000 hr ($12.70 per LED)
Error	±1 % light ripple ± 15 % lamp to lamp error	±10 % LED to LED error
Cost	~ $ 10,000	$ 125 single LED $ 55 per additional LED

[a]Applies to white and warm white LEDs only

the range of 425-775 nm. The LEDs are nearly monochromatic with full width at half max (FWHM) values of 20 nm. LEDs cost 2 % that of a Xe bulb yet have a lifetime of 100 times that of a Xe bulb. A typical research grade 1000 W Xe arc lamp system costs ~$ 10,000 as compared to an LED systems such as the 3rd generation array, which costs $125 for the first LED and $ 55 for each additional LED with the difference due to one time purchases such as a power supply. The total cost of the 3rd generation array is $ 565, which equates to ~5 % of the cost of a single 1000 W Xe arc lamp or 0.7 % of the cost of an equivalent 8 lamp system. Recently, Bernhard[48] engineered a high-throughput photolysis system utilizing Luxeon LEDs. Citing all the advantages of LEDs Bernhard constructed an eight LED array powered by a Xitanium constant current driver. Bernhard used the LED array to investigate Ir photosensitizers in solar hydrogen production. This system appeared to have reproducibility issues. The present study is a thorough evaluation of LED array photolysis systems in terms of precision and method validation

as such a study is unprecedented in the literature. This is followed by sequential improvement to produce a high throughput photolysis system.

3.7 Actinometric Evaluation

The LEDs are treated as uniform in the data analysis. As such, precision is evaluated within each series of measurements to determine if the assumption of uniformity is supported. Analysis of variance, ANOVA, calculations are made between the different LEDs, at 95 % confidence, to determine if there is a statistically significant difference between the outputs of the LEDs in the arrays. There are two main considerations when using ANOVA to determine differences in sets of data. First, as with general statistics for ANOVA calculation to be valid the data must be normally distributed. If the data are not normally distributed, other statistical methods must be employed. All the data for each experiment were evaluated in the form of Rankit plots. The Rankit method plots the data (x-axis) against the value, z, of the normal probability function associated with the cumulative frequency of the data. Normally distributed data would be approximately linear in a Rankit plot. The Rankit plots for each experiment are included in the appendix. All the data appeared normally distributed.

The second consideration when relying on ANOVA calculations to infer statistical significance of the difference between sets of data comes from the calculation of the F (Fisher) number shown again in equation 3.1.

$$F = \frac{MS_L}{MS_E} \tag{3.1}$$

As can be seen the F number depends on the ratio of the MS_L the mean squares of the variance between data sets to MS_E the mean squares of the variance within the data sets. As the variance within the data sets increases relative to the variance between the data sets, the F number gets smaller, increasing the likelihood of a statistically insignificant result. This would be a type II, which is finding no difference when there really is one.

As the percent error in the experiments increases, the likelihood of a type II error increases.

3.7.1 Actinometric Evaluation of the 1st Generation LED Array

Using an LED for photochemistry requires that a design be determined that provides the needed level of reproducibility for any application. Our first generation LED array was constructed in the simplest manner after Bernhard's array and then evaluated using calorimetric measurements. The first generation LED array uses five LEDs wired in parallel with a single resistor for power management. The calorimetric measurements performed are useful for evaluation because they remove errors introduced in more complex photochemical reactions like H_2 production. The LEDs in this design are not individually controllable. Calorimetric measurements provide a convenient tool to observe precision. Table 3.4 displays three sample power measurements for each of the five 470 nm Prolight 5 W LEDs in the first generation LED array. For the first generation

array the descriptive statistical analysis within the three trials indicate that there is low precision between the LEDs. The coefficient of variance for the three trials indicates that the scatter about the mean of one standard deviation is greater than 7%. The confidence integrals reinforce the low precision as they represent greater than 9% of the mean value. The data was also evaluated using ANOVA with F and F_{crit} calculated as 45.1 and 3.48, respectively, indicating that there is a statistically significant difference between the powers measured from the LEDs in the first generation LED array. The low precision for this first generation system may result from the LEDs, which are non-linear devices, being wired in parallel with a common resistor, allowing power to be unevenly distributed amongst the LEDs.

Table 3.4 First generation LED array calorimetric measurements for five 470 nm Prolight 5 W LEDs

replicate	LED 1	LED 2	LED 3	LED 4	LED 5	mean	CV[a] (%)	CL[b] (95%)
1 (W)	0.050	0.052	0.056	0.063	0.056	0.055	9.1	0.0062
2 (W)	0.048	0.051	0.058	0.063	0.055	0.055	10.7	0.0073
3 (W)	0.051	0.050	0.056	0.060	0.055	0.054	7.5	0.0050

[a]coefficient of variance. [b]confidence integral evaluated at 95%

	F	F_{crit}
ANOVA	45.1	3.48

Table 3.5 Second generation LED array calorimetric measurements for five 470 nm Prolight 5 W LEDs

replicate	LED 1	LED 2	LED 3	LED 4	LED 5	Mean	CV (%)	CL (95%)
1 (W)	0.056	0.056	0.058	0.056	0.060	0.057	3.5	0.0024
2 (W)	0.056	0.054	0.056	0.057	0.060	0.056	4.1	0.0029
3 (W)	0.056	0.055	0.056	0.058	0.059	0.056	3.7	0.0026

[a]coefficient of variance. [b]confidence integral evaluated at 95%

	F	F_{crit}
ANOVA	12.4	3.48

3.7.2 Actinometric Evaluation of the 2nd Generation LED Array

The results of the analysis of power output for the first generation LED array system indicated that modifications were needed to improve reproducibility. A second generation array was constructed that wired five LEDs in parallel series, each with their own resistor (± 1 % tolerance) for power management. The second generation LED array was evaluated using both calorimetric measurements and chemical actinometry shown in Tables 3.5 and 3.6, respectively. When compared to the first generation LED array, the second generation LED array displays improved precision. The coefficient of variance has been decreased by a factor of three. The confidence integrals are roughly three times smaller illustrating that the measurements are grouped closer to the mean. ANOVA yields F and F_{crit} values of 12.4 and 3.48, respectively, which is an improvement from the first generation LED array. The ANOVA results indicate there is a statistically significant difference between the LEDs with low probability of this occurring by chance. As shown in Table 3.6 the second generation LED array was evaluated using chemical actinometry. It is noticed that there is more error in these experiments due to the more complex experimental procedure. The results of the actinometry experiments indicate precision varied from two to ten percent in the coefficient of variance, and the confidence integrals ranged from three to twelve percent of the mean. ANOVA calculations reinforced the results from the calorimetric measurements with F and F_{crit} equal to 3.80 and 3.48, respectively.

Table 3.6 Second generation LED array tris(oxalato)ferrate(III) chemical actinometry experiments for five 470 nm Prolight 5 W LEDs

replicate	LED 1	LED 2	LED 3	LED 4	LED 5	mean	CV (%)	CL (95%)
1 ($\times 10^{18}$ quanta min^{-1})	3.80	3.80	3.71	4.00	3.78	3.82	2.8	0.13
2 ($\times 10^{18}$ quanta min^{-1})	3.76	3.67	3.64	4.13	3.73	3.78	5.2	0.25
3 ($\times 10^{18}$ quanta min^{-1})	3.76	3.67	3.67	4.43	4.36	3.76	10.2	0.45

[a]coefficient of variance. [b]confidence integral evaluated at 95%

	F	F_{crit}
ANOVA	3.8	3.48

Table 3.7 Third generation LED array calorimetric measurements for four 530 nm Prolight 5 W LEDs

Replicate	LED 1	LED 2	LED 3	LED 4	mean	CV (%)	95% CL
1 (W)	0.082	0.080	0.079	0.082	0.081	1.90	0.0024
2 (W)	0.081	0.080	0.078	0.080	0.080	1.60	0.0020
3 (W)	0.080	0.081	0.080	0.080	0.080	0.06	0.0008

[a]coefficient of variance. [b]confidence integral evaluated at 95%

	F	F_{crit}
ANOVA	2.52	4.07

statistically significant difference between the LEDs in the second generation LED array. One reason for the improved precision relative to the first generation LED array is the circuit improvement made by accomplishing power restriction in series with each LED in the array.

3.7.3 Actinometric Evaluation of the 3rd Generation LED Array

The results of the analysis of the first and second generation arrays indicated that improvements were needed to achieve a sufficiently precise photolysis system using LED light sources. A third generation array was constructed using information gained in the statistical analysis of the first two systems. The third generation system allowed for power management for each of the eight LEDs and provides thermostated control of sample temperature. The third generation LED array was evaluated using calorimetric measurements and chemical actinometry. Table 3.7 shows the results of the calorimetric measurements. Calorimetric measurements were taken by adjusting the calorimetric measurements of four 530 nm Prolight 5 W LEDs to the same value, and subsequently monitoring this value over a period of weeks without readjustment. In practice the LEDs in the array are set to the same value making evaluation by calorimetric measurements meaningless. The purpose of this experiment was to monitor the long term stability of the LED output using this circuit. As can be seen, the coefficient of variance is about half that for the second generation LED array and the confidence limits improve. ANOVA analysis calculations show that there is no statistically significant difference between the LED calorimeter measurements with F and F_{crit} equal to 2.52 and 4.07, respectively.

Table 3.8 Third generation LED array tris(oxalato)ferrate(III) chemical actinometry experiments with three 470 nm Luxeon V 5 W LEDs

replicate	LED 1	LED 2	LED 3	mean	CV (%)	CL (95%)
1 ($\times 10^{18}$ quanta min^{-1})	9.70	9.32	9.04	9.32	3.5	0.82
2 ($\times 10^{18}$ quanta min^{-1})	8.96	9.39	9.62	9.10	3.6	0.83
3 ($\times 10^{18}$ quanta min^{-1})	9.66	8.56	9.09	9.10	6.0	1.37

[a]coefficient of variance. [b]confidence integral evaluated at 95%

	F	F_{crit}
ANOVA	3.8	3.48

The result illustrates a significant advantage of having a controllable LED output in the third generation array. Table 3.8 contains the results from chemical actinometry experiments performed with the third generation LED array.

It must be noted that actinometry performed with the third generation LED array utilized Philips Lumileds Lighting Company Luxeon V 5 W LEDs. Prolight Opto Technology Corporation and Philips Lumileds Lighting Company report the same photometric output for their respective 470 nm, 5 W LEDs indicating that there should be no differences between the respective LED operations. It can be seen from Table 3.8 that the precision is roughly the same for two replicates, but half as precise for the third replicate when compared to the second generation LED actinometry results. ANOVA calculations report F and F_{crit} values of 0.566 and 5.14, respectively, indicating that there is no statistically significant difference between the actinometry results of the LEDs evaluated. This is an exciting result indicating that different photochemical experiments could be performed with each of the LEDs in the array allowing for multiplexing. This

freedom allows the experimenter the ability to use high throughput effects of the eight LEDs in the third generation LED array.

3.7.4 Actinometric Evaluation Constant Current Drivers

Constant current drivers were evaluated as power sources for the 3rd generation LED array. Constant current drivers were evaluated because the drivers provide a simpler circuit and are less expensive. Constant current drivers provide a fixed current to the LED thus eliminating the need for the power limiting resistor that is required in a constant voltage system. The constant current driver is less expensive than the power supply and requires fewer electrical components, which results in a 44 % decrease in cost per LED. Two manufacturer suggested drivers, were investigated as a power source for the third generation LED array. In these experiments the array was set up as normal with only the power source changing. The LEDs were evaluated by measuring the output with the power meter as the load changed by addition of LEDs into the circuit. The first experiment used a Xitanium Driver (25 W, 1050 mA), which powers up to 8 LEDs in two parallel series of 4 LEDs. Figure 3.6 shows the power output of the LEDs as the number of LEDs in the circuit was increased from two to eight. The number of LEDs was increased in even number increments. It was found that an odd number of LEDs results in two unsymmetrical series in parallel, which causes a power shift to the series with the smaller load.

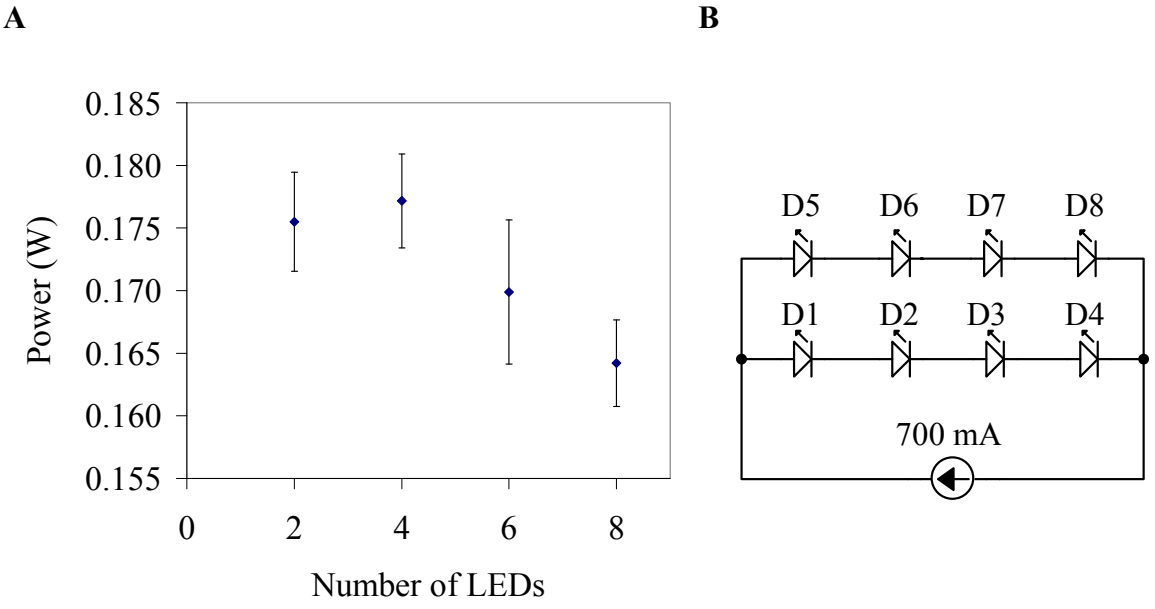

Figure 3.6 A. Power output of LEDs in the 3rd generation LED array as driven by a Xitanium Driver (25 W, 1050 mA). Power was measured by a calorimeter. **B.** Circuit diagram of LEDs in the 3rd generation LED array as driven by a Xitanium Driver (25 W, 1050 mA).

The result of the load difference was that the low load series was powered at 1000 mA, and the high load series was powered at 50 mA, as measured by a digital multimeter. As can be seen from Figure 3.6 there is a 10 % drop in power as the circuit load was increased from two to eight LEDs. This drop in power would result in an unacceptable difference in photon flux, which is completely dependent on the number of LEDs in the circuit. The second driver evaluated was a Xitanium Driver (17 W, 700 mA), which powers up to 4 LEDs in series. Figure 3.7 shows the power output of the LEDs as the number of LEDs in the circuit was increased from one to four.

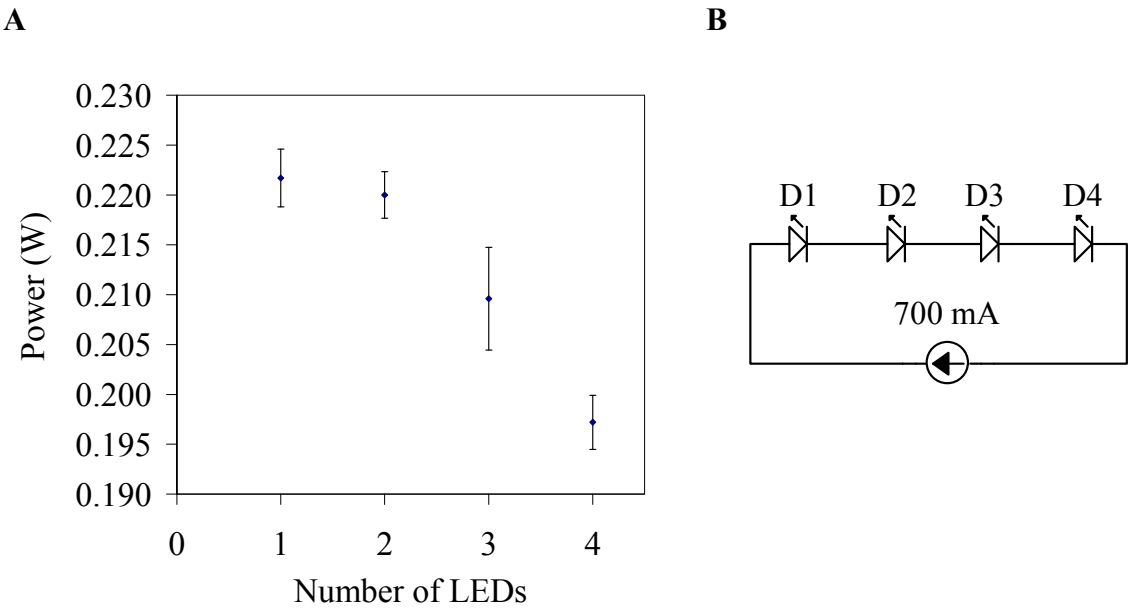

Figure 3.7 A. Power output of LEDs in the 3rd generation LED array as driven by a Xitanium Driver (17 W, 700 mA). Power was measured by a calorimeter. **B.** Circuit diagram of LEDs in the 3rd generation LED array as driven by a Xitanium Driver (17 W, 700 mA).

As can be seen from Figure 3.7 there is a 9 % drop in power as the circuit load was increased from one to four LEDs. This drop in power would result in an unacceptable difference in photon flux, which is completely dependent on the number of LEDs in the circuit.

3.7.5 Actinometric Evaluation of Xe Arc Lamp

Chemical actinometry performed with the Xe arc lamp for comparison purposes is presented in Table 3.9. It is shown that the precision from the lamp is

comparable to that of the LED arrays. The coefficient of variance is five percent, and the confidence integral is eight percent relative to the mean. Furthermore, the third

Table 3.9 Tris(oxalato)ferrate(III) chemical actinometry performed with a 1000 W Xe arc lamp

replicate	Xe arc lamp
1 ($\times 10^{18}$ quanta min^{-1})	1.76
2 ($\times 10^{18}$ quanta min^{-1})	1.62
3 ($\times 10^{18}$ quanta min^{-1})	1.58
4 ($\times 10^{18}$ quanta min^{-1})	1.60
mean	1.64
CV (%)	5.0
CL (95%)	0.13

generation LED array emits 5.6 times the photons per minute as the 1000 W Xe arc lamp when filtered to 460 nm with a narrow band pass filter. Thus, the array is comparable in both precision and photonic output to the Xe arc lamp supporting the advantages of an LED system for high-throughput analysis.

3.8 Photocatalytic Hydrogen Production

The supramolecular complex $[\{(bpy)_2Ru(dpp)\}_2RhCl_2](PF_6)_5$ is a device for photoinitiated electron collection. The Rh core can collect multiple electrons or reducing equivalents when photolyzed in the presence on an electron donor such as dimethylaniline.[43] Following electron collection and conversion from the 18 e^- d^6 psuedo octahedral complex to a 16 e^- d^8 square planar complex the supramolecular architecture

remains intact. This is unprecedented in the literature. The supramolecular assembly is a prime choice for a multi-electron homogeneous catalyst for small molecule activation such as solar hydrogen production. Following the method development and validation according to actinometric measurements the complex functioning, with respect to catalytic solar hydrogen production from water in the presence of dimethylaniline (DMA) was investigated using the 3rd generation LED array. Studies were performed such that the supramolecular complex $[\{(bpy)_2Ru(dpp)\}_2RhCl_2](PF_6)_5$ was photolyzed with the 3rd generation LED array in a solution of 7:1 acetonitrile/water with added DMA. Table 3.10 gives the experimental parameters used. Upon photolysis the production of the Rh^I form of the complex, $[\{(bpy)_2Ru(dpp)\}_2Rh^I]^{5+}$, is observed. Following the change in the spectroscopy to that characteristic of the Rh^I complex, H_2 evolution is observed. The data in Table 3.11 shows the results of photochemical hydrogen production using the photocatalyst $[\{(bpy)_2Ru(dpp)\}_2RhCl_2](PF_6)_5$ in CH_3CN:H_2O solution with DMA as the electron donor. The solution was photolyzed for two hours using the optimized 3rd generation LED array.

Table 3.10 Experimental conditions for solar hydrogen production studies with the supramolecular complex $[\{(bpy)_2Ru(dpp)\}_2RhCl_2](PF_6)_5$

component	concentration
$[\{(bpy)_2Ru(dpp)\}_2RhCl_2]^{5+}$	80 μM
DMA	0.89 M
Water (pH 2, HCl)	6.2 M, 11 % v/v
solution volume	4.5 mL
headspace	1.0 mL

Table 3.11 Photochemical hydrogen production using the photocatalyst $[\{(bpy)_2Ru(dpp)\}_2RhCl_2](PF_6)_5$ in a 7:1 $CH_3CN:H_2O$ solution with dimethylaniline as the electron donor. The solution was photolyzed for two hours with using the 3rd generation LED array with 530 nm LEDs. Statistical analysis of results is given (bpy = 2,2'-bipyridine and dpp = 2,3-bis(2-pyridyl)pyrazine).

530 nm (2hr)	LED 1	LED 2	LED 3	LED 4	mean	CV (%)	CL (95%)
H_2 prod (μL) 1	15.04	14.19	15.40	16.01	15.16	5.02	1.21
H_2 prod (μL) 2	18.26	16.23	17.37	17.12	17.24	4.84	1.33

530 nm	F stat.	F crit.
H_2 prod	0.367	6.591

Table 3.12 Photochemical hydrogen production using the photocatalyst $[\{(bpy)_2Ru(dpp)\}_2RhCl_2](PF_6)_5$ in a 7:1 $CH_3CN:H_2O$ solution with dimethylaniline as the electron donor with photolysis for one, two and four hours using the 3rd generation LED array with 530 nm LEDs. Statistical analysis of results is given (bpy = 2,2'-bipyridine and dpp = 2,3-bis(2-pyridyl)pyrazine).

530 nm	LED 1	LED 2	LED 3	LED 4	mean	CV (%)	CL (95%)
H_2 prod (μL) 1hr	8.56	9.21	8.22	8.86	8.71	4.85	0.67
H_2 prod (μL) 2hr	18.26	16.23	17.37	17.12	17.24	4.84	1.33
H_2 prod (μL) 4hr	36.60	37.90	35.30	36.90	36.67	2.92	1.71

530 nm	F stat.	F crit.
LEDs	0.602	4.757
over time	1055	5.143

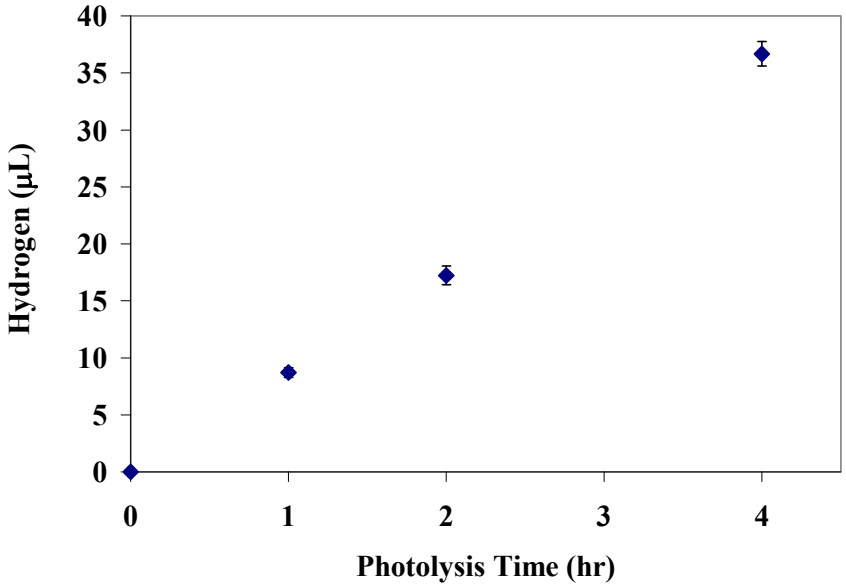

Figure 3.8 Photochemical hydrogen production using the photocatalyst $[\{(bpy)_2Ru(dpp)\}_2RhCl_2](PF_6)_5$ in CH_3CN/H_2O solution with dimethylaniline as the electron donor with photolysis for one, two and four hours using an optimized LED array (bpy = 2,2'-bipyridine and dpp = 2,3-bis(2-pyridyl)pyrazine).

Statistical analysis shows that the precision is five percent, a respectable figure as the array precision determined by actinometry is three percent. Furthermore, ANOVA calculations yield an F value of 0.367 and an F_{crit} 6.591 suggesting that there is no statistically significant difference between the experimental results. This result points to the ability to use each LED as an independent light source for H_2 production photochemistry allowing for high-throughput investigations. Table 3.12 and Figure 3.8 show the production of H_2 by the photocatalyst $[\{(bpy)_2Ru(dpp)\}_2RhCl_2](PF_6)_5$ in a 7:1 $CH_3CN:H_2O$ solution with DMA as the electron donor as a function of photolysis time. It can be seen that the photocatalyst produces H_2 linearly with time and that there is no

statistically significant difference between LEDs in this application. Furthermore, H_2 production is shown to be statistically different as photolysis time is increased an expected result for an active photocatalytic system.

Chapter 4. CONCLUSIONS AND FUTURE WORK

Photochemical research is essential to understand light energy conversion. The use of LEDs will allow for the detailed analysis of factors impacting photochemical reactions. The successful implementation of LEDs as a light source for photochemical conversions requires the analysis of the stability and reproducibility of this light source in photochemical reactions. In the present study three LED array systems utilizing ultra high intensity LEDs have been constructed and evaluated for precision and variance. The LED arrays were compared with a traditional photochemical light source, a 1000 W Xe arc lamp. The optimized 3rd generation LED array was used to determine the effect of the power supply. The optimized 3rd generation LED array was used as the photolysis source in photochemical hydrogen production studies implementing supramolecular catalysts. The analysis indicates that the circuitry as well as the instrument design is of great importance.

The first generation LED array is wired in parallel to provide an LED array costing less than $ 200, or 0.2 % the cost of a Xe arc lamp. However, it was shown to be the least precise array studied with greater than 7 % error. The high error is better than the manufacturer's rated precision and the precision of LED arrays found in the literature,[34] but too high to use for most photochemical analyses. The first generation LED array was shown to provide statistically different light outputs by analysis of

variance, ANOVA. If implemented in photochemical research the result of photolysis would depend on the LEDs used.

The second generation LED array maintained the benefits of affordability costing less than $ 200, or 0.2 % the cost of a Xe arc lamp. The precision of the 2nd generation LED array with respect to the 1st generation LED array was greatly improved. The coefficient of variance decreased from greater than 7 % to less than 4 % as evaluated by calorimetric measurements. The increase in precision is most likely due to applying power restriction in series rather than parallel. The second generation LED array was also evaluated by chemical actinometry. Chemical actinometry experiments reported error ranging from 3 – 10 %. This is in part due to the added complexity of the experiment. The data were evaluated to check for outliers, but all the data were shown to be part of the normal distribution by Grubbs test. Also, the second generation LED array was shown to provide statistically different light outputs according to ANOVA calculations with respect to both the calorimetric and actinometric evaluations.

The third generation LED array maintained the benefits of affordability with a cost of $ 565 which equates to ~5 % of the cost of a 1000 W Xe arc lamp. The 3rd generation array is vastly different from the 1st and 2nd generations allowing for enhanced user control. By design the third generation array allows for LED modulation with any 5 W Luxeon or Prolight LED; an option unavailable in the first two generations. The array also allows for control with respect to the number of LEDs operated, and can power up to eight different LEDs. The array also provides for thermostating. The success of the 3rd generation LED array with respect to photochemical performance is due to the circuitry.

By design the array allows for light output calibration with any Luxeon or Prolight 5 W LED. Calibration of light output is made possible by the use of power limiting resistors, and rheostats for fine tuning of the LED output. For this reason the 3rd generation LED array was shown to be the most precise. The third generation LED array displayed long term stability. Calorimetric measurements showed no substantial increase in error over a period of three weeks. Chemical actinometry experiments reported an error of 4-6 %, which is more precise than the respective 2nd generation array actinometry experiments. Also, the optimized third generation array was the only LED array tested which ANOVA calculations supported as having no statistically significant difference between the LEDs in the array. The implications of this result are significant. Photochemical research can be performed with the optimized LED array without any difference in photolysis due to the LEDs used. The third generation optimized LED array was shown to be comparable in both precision and photonic output to a conventional 1000 W Xe arc lamp when filtered to 460 nm with a narrow band pass filter. The output of the optimized array was found to five times larger than that of the filtered Xe arc lamp.

The optimized validated LED array was implemented in photocatalytic hydrogen production studies. The supramolecular device for photoinitiated electron collection, $[\{(bpy)_2Ru(dpp)\}_2RhCl_2](PF_6)_5$, was photolyzed in solution with water and dimethylaniline, an electron donor. Hydrogen production was shown to be linear with time. Analysis of variance calculations confirmed that there is no statistically significant difference between the results of photolysis for all studies performed. Two way analysis of variance showed that there is no statistically significant difference within any of the

photolyses, but that the results between different photolyses in the time study provided statistically different results. This result is typical of a photocatalytic system.

A valid method of photolysis has been developed with respect to the optimized LED array. This study was performed such that a valid method of high-throughput photochemistry might be developed and applied in studies of supramolecular catalysts for hydrogen production. Current studies are in progress using the array as a tool to modulate reaction conditions and evaluate the impact of these perturbations. Perturbations such as modulating the nature of the supramolecular complex, electron donor, water source, pH, solvent, reaction temperature, the wavelengths and intensity of the light source will be made in an attempt to understand catalyst functioning and reaction mechanism .

REFERENCES

(1) Bird, R. E.; Hulstrom, R. L.; Lewis, L. J. *Sol. Energy* **1983**, *30*, 563.

(2) Zamaraev, K. I.; Parmon, V. N. *Catal. Rev.-Sci. Eng.* **1980**, *22*, 261-324.

(3) http://www.eia.doe.gov/oiaf/ieo/world.html.

(4) Balzani, V.; Moggi, L.; Manfrin, M. F.; Bolletta, F.; Gleria, M. *Science* **1975**, *189*, 852-856.

(5) Bolton, J. R. *Science* **1978**, *202*, 705-711.

(6) Huheey, J. E.; Keiter, E. A.; Keiter, R. L. *Inorganic Chemistry: Priciples of Structure and Reactivity*; 4 ed.; HarperCollins College Publishers: New York, 1993.

(7) Amouyal, E. *Sol. Energy Mater. Sol. Cells* **1995**, *38*, 349-276.

(8) Bard, A. J.; Fox, M. A. *Acc. Chem. Res.* **1995**, *28*, 141-145.

(9) Braunstein, C. H.; Baker, A. D.; Strekas, T. C.; Gafney, H. D. *Inorg. Chem.* **1984**, *23*, 857-864.

(10) Brown, G. M.; Brunschwig, B. S.; Creutz, C.; Endicott, J. F.; Sutin, N. *J. Am. Chem. Soc.* **1979**, *101*, 1298-1300.

(11) Chan, S. F.; Chou, M.; Creutz, C.; Matsubara, T.; Sutin, N. *J. Am. Chem. Soc.* **1981**, *103*, 369-379.

(12) Brown, G. M.; Brunschwig, B. S.; Creutz, C.; Endicott, J. F.; Sutin, N. *Journal of the American Chemical Society* **1979**, *101*, 1298-1300.

(13) Krishnan, C. V.; Brunschwig, B. S.; Creutz, C.; Sutin, N. *J. Am. Chem. Soc.* **1985**, *107*, 2005-2015.

(14) Molnar, S. M.; Nallas, G.; Bridgewater, J. S.; Brewer, K. J. *J. Am. Chem. Soc.* **1994**, *116*, 5206-5210.

(15) Dasgupta, P. K.; Bellamy, H. S.; Liu, H.; Lopex, J. L.; Loree, E. L.; Morris, K.; Petersen, K.; Mir, K. A. *Talanta* **1993**, *40*, 53-74.

(16) Adivarahan, V.; Wu, S.; Chitnis, A.; Pachipulusu, R.; Mandavilli, V.; Shatalov, M.; Zhang, J. P.; Khan, M. A.; Tamulaitis, G.; Sereika, A.; Yilmaz, I.; Shur, M. S.; Gaska, R. *Appl. Phys. Lett.* **2002**, *81*, 3666-3668.

(17) http://www.lumileds.com.

(18) Gennett, T.; Milner, D. F.; Weaver, M. J. *J. Phys. Chem.* **1985**, *89*, 2787-2794.

(19) Swavey, S.; Brewer, K. J. *Inorg. Chem.* **2002**, *41*, 4044-4050.

(20) Kuhn, H. J.; Braslavsky, S. E.; Schmidt, R. *Pure Appl. Chem.* **2004**, *76*, 2105-2146.

(21) http://www.scientech-inc.com/laserpower.phtml.

(22) Parker, C. A. *Proc. R. Soc. London, Ser. A* **1953**, *220*, 104-116.

(23) Parker, C. A. *Trans. Faraday Soc.* **1954**, *50*, 1213-1221.

(24) Hatchard, C. G.; Parker, C. A. *Proc. R. Soc. London, Ser. A* **1956**, *235*, 518-536.

(25) Parker, C. A.; Hatchard, C. G. *J. Phys. Chem.* **1959**, *63*, 22-26.

(26) Demas, J. N.; Bowman, W. D.; Zalewski, E. F.; Velapoldi, R. A. *J. Phys. Chem.* **1981**, *85*, 2766-2771.

(27) Baxendale, J. H.; Bridge, N. K. *J. Phys. Chem.* **1955**, *59*, 783-788.

(28) Parker, C. A. *Photoluminescence of Solutions*; Elsevier: Amsterdam, 1968.

(29) Burgess, J.; Haines, R. I. *J. Chem. Eng. Data* **1978**, *23*, 196-197.

(30) Kirk, A. D.; Namasivayam, C. *Anal. Chem.* **1983**, *55*, 2428-2429.

(31) Lee, J.; Seliger, H. H. *J. Chem. Phys.* **1964**, *40*, 519-523.

(32) Molnar, S. M., Virginia Polytechnic Institute and State University, 1996.

(33) Rillema, D. P.; Allen, G.; Meyer, T. J.; Conrad, D. *Inorg. Chem.* **1983**, *22*, 1617-1622.

(34) Goldsmith, J. I.; Hudson, W. R.; Lowry, M. S.; Anderson, T. H.; Bernhard, S. *J. Am. Chem. Soc.* **2005**, *127*, 7502-7510.

(35) Molnar, S. M.; Jensen, G. E.; Vogler, L. M.; Jones, S. W.; Laverman, L.; Bridgewater, J. S.; Richter, M. M.; Brewer, K. J. *J. Photochem. Photobiol., A* **1994**, *80*, 315-322.

(36) Purwanto; Deshpande, R. M.; Chaudhari, R. V.; Delmas, H. *J. Chem. Eng. Data* **1996**, *41*, 1414-1417.

(37) Skoog, D.; West, D. M.; Holler, J. F.; Crouch, S. R. *Analytical Chemistry: An Introduction*; 7th ed.; Saunders College Publishing: New York, 2000.

(38) Hibbert, D. B.; Gooding, J. J. *Data Analysis for Chemistry: An Introductory Guide for Students and Laboratory Scientists*; Oxford University Press: New York, 2006.

(39) Weiss, D. J. *Analysis of Variace and Functional Measurement: A Practicle Guide*; Oxford University Press: New York, 2006.

(40) Brewer, K. J.; Murphy, W. R.; Spurlin, S. R.; Petersen, J. D. *Inorg. Chem.* **1986**, *25*, 882-884.

(41) Richter, M. M.; Brewer, K. J. *Inorg. Chem.* **1992**, *31*, 1594-1598.

(42) Kew, G.; DeArmond, M. K.; Hanck, K. W. *J. Phys. Chem.* **1974**, *78*, 727-734.

(43) Elvington, M.; Brewer, K. J. *Inorg. Chem.* **2006**, *45*, 5242-5244.

(44) Elvington, M.; Brown, J. R.; Zigler, D. F.; Brewer, K. J.; Lionel, V., Ed.; SPIE: 2006; Vol. 6340, p 63400W.

(45) Nocera, D. G.; Dempsey, J. L.; Esswein, A. J.; Manke, D. R.; Rosenthal, J.; Soper, J. D. *Inorg. Chem.* **2005**, *44*, 6879-6892.

(46) Rasmussen, S. C.; Richter, M. M.; Yi, E.; Place, H.; Brewer, K. J. *Inorg. Chem.* **1990**, *29*, 3926-3932.

(47) Brewer, K. J.; Elvington, M. 2006; Vol. US 7,122,171 B2.

(48) Bernhard, S. G., Jonas I.; Hudson, William R.; Lowry, Micheal S.; Anderson, Timothy H. *J. Am. Chem. Soc.* **2005**, *127*, 7502-7510.

APPENDIX A: Representative Hydrogen Calibration Curve

This Appendix includes a representative hydrogen calibration curve used with the gas chromatograph for the accurate determination of hydrogen in the injection sample. Calibration curves were obtained once a month, or anytime a test aliquot of hydrogen yielded a result which varied 10% or more from the nominal value.

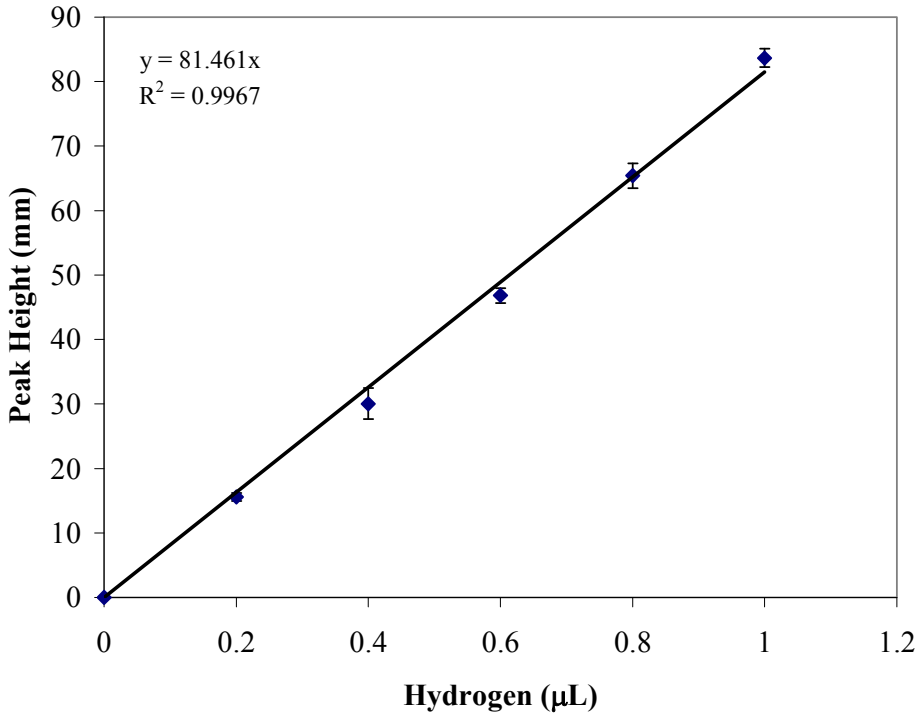

Figure A.1. Representative hydrogen calibration curve.

APPENDIX B: Statistical Evaluation of Data

This Appendix includes statistical evaluations of raw data in the form of rankit plots and Grubbs test plots. The rankit plots or normal distribution plots are used to evaluate the normality of the data. In a rankit plot, if the data are normally distributed than the plot should resemble a straight line. In Gubbs test plots, the data median value is represented by a solid line, and the dashed line represents the closest value at which an outlier would appear at 95% probability.

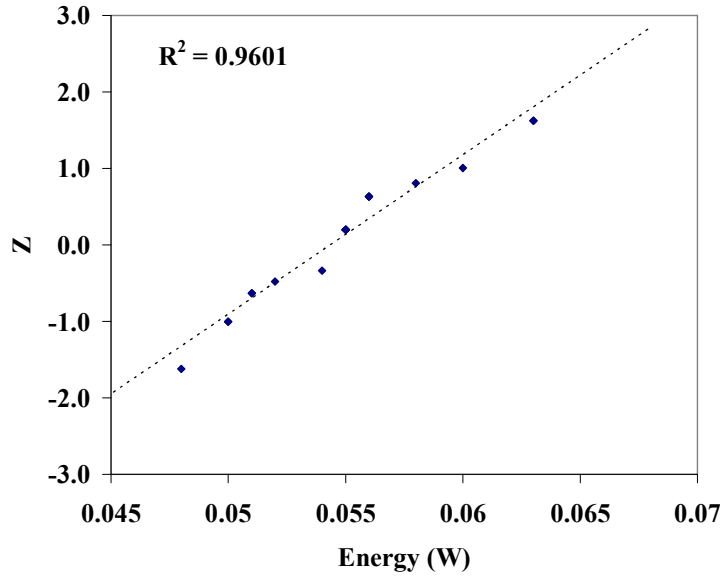

Figure B.1. Rankit plot for the 1st generation LED array calorimetry experiment. Data appear to be normally distributed.

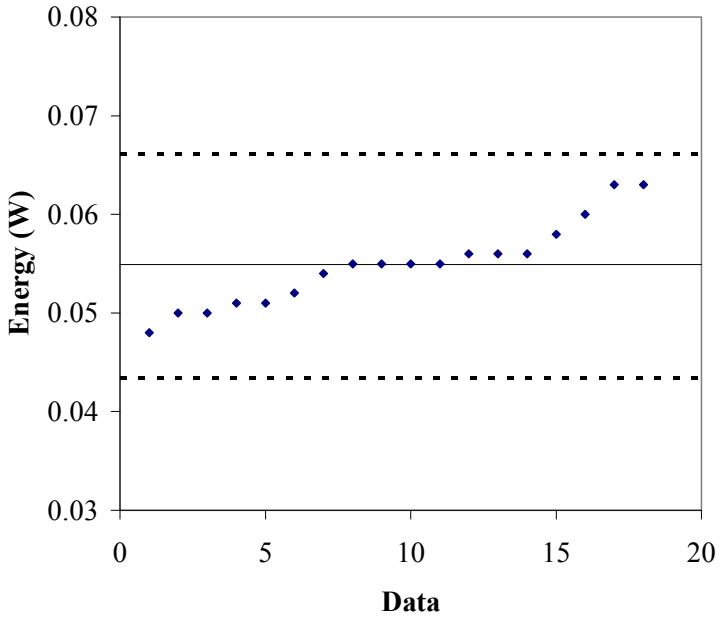

Figure B.2. Plot of the 1st generation LED array calorimetry experiment data. Dashed lines represent where outliers would be present according to the Grubbs test

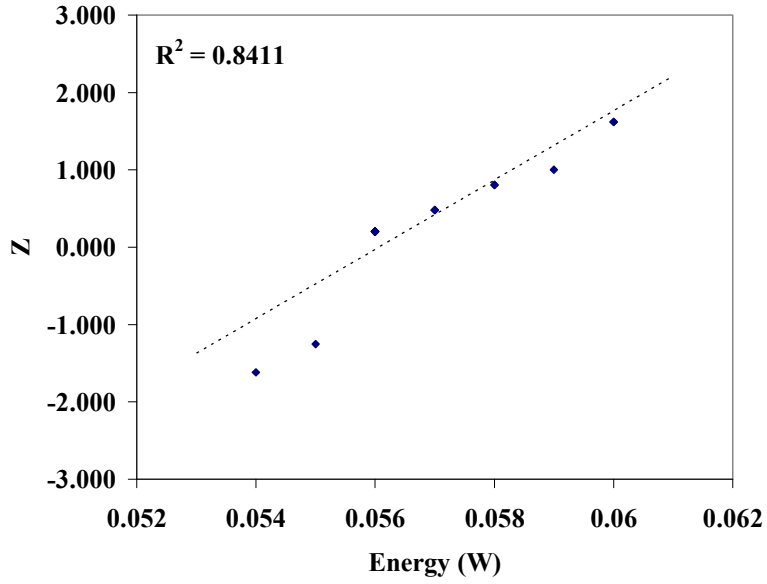

Figure B.3. Rankit plot for the 2nd generation LED array calorimetry experiment. Data appear to be normally distributed.

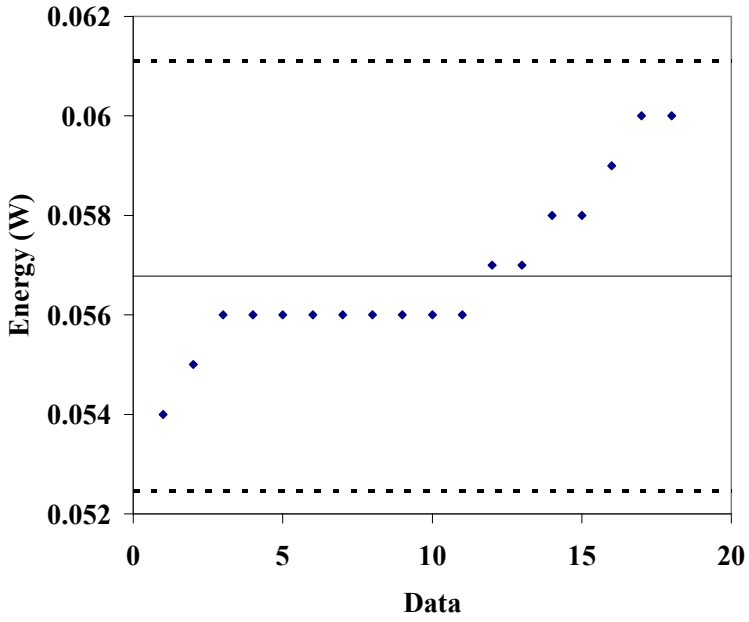

Figure B.4. Plot of the 2nd generation LED array calorimetry experiment data. Dashed lines represent where outliers would be present according to the Grubbs test

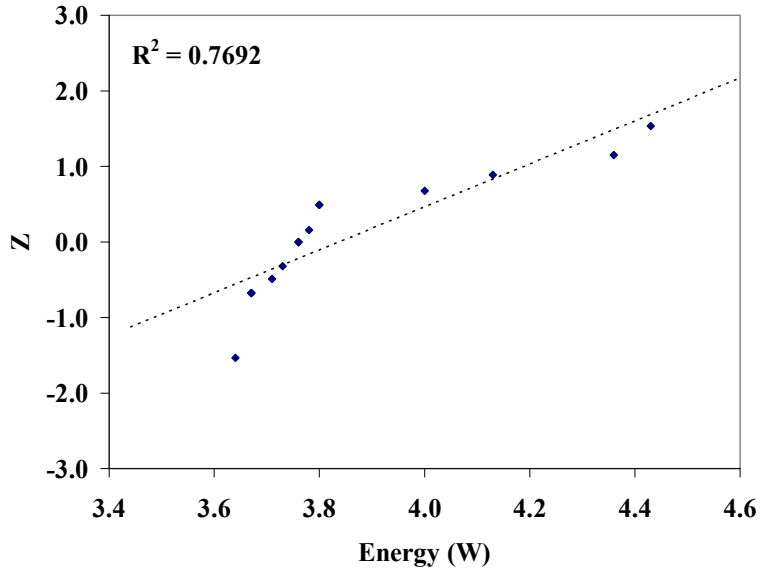

Figure B.5. Rankit plot for the 2nd generation LED array actinometry experiment. Data appear to be normally distributed

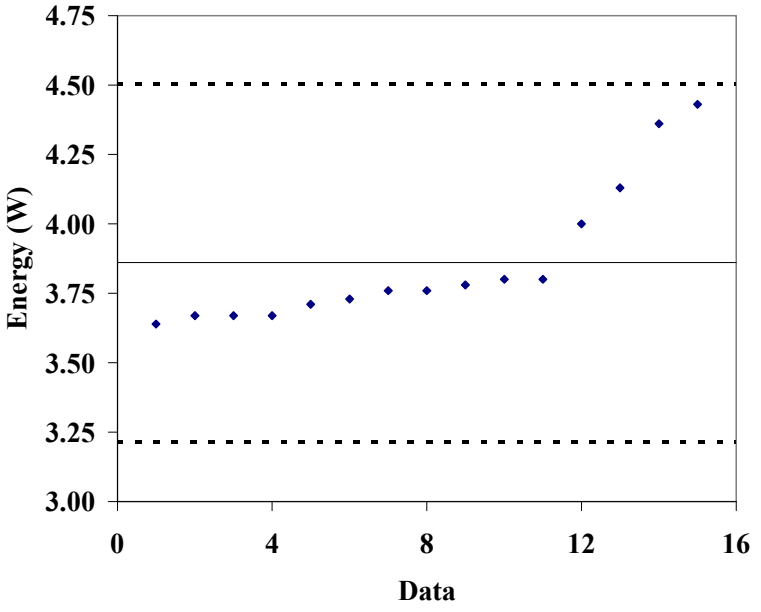

Figure B.6. Plot of the 2nd generation LED array actinometry experiment data. Dashed lines represent where outliers would be present according to the Grubbs test

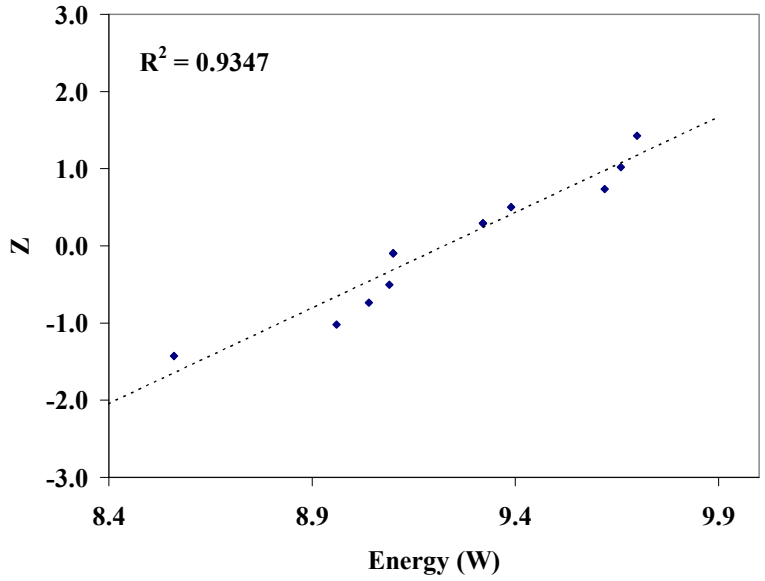

Figure B.7. Rankit plot for the 3rd generation LED array actinometry experiment. Data appear to be normally distributed

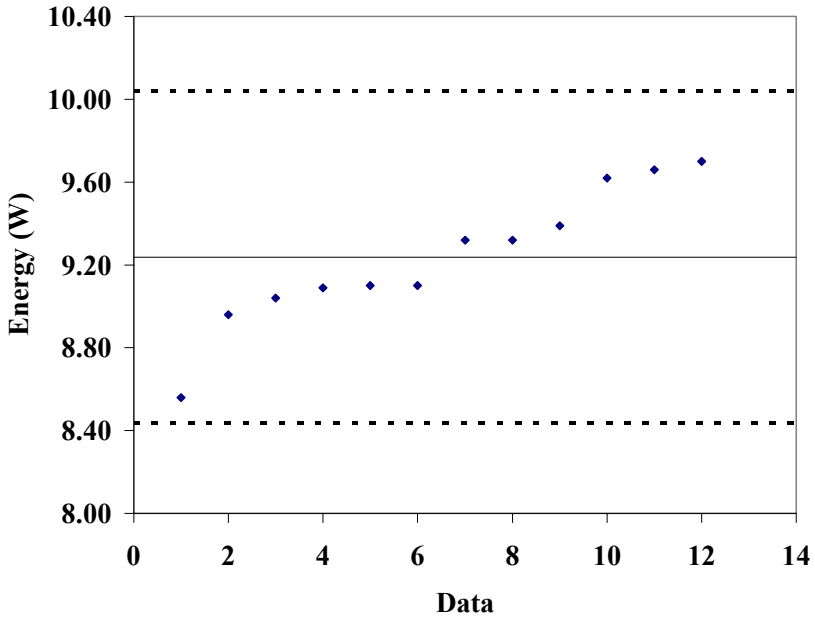

Figure B.8. Plot of the 3rd generation LED array actinometry experiment data. Dashed lines represent where outliers would be present according to the Grubbs test

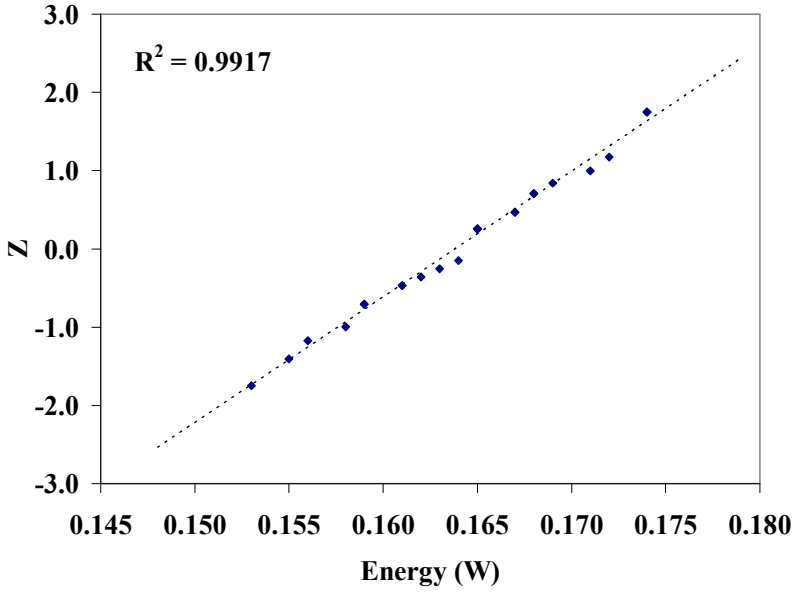

Figure B.9. Rankit plot for the 3rd generation LED array calorimetry experiment investigating the 8 LED constant current driver. Data appear to be normally distributed

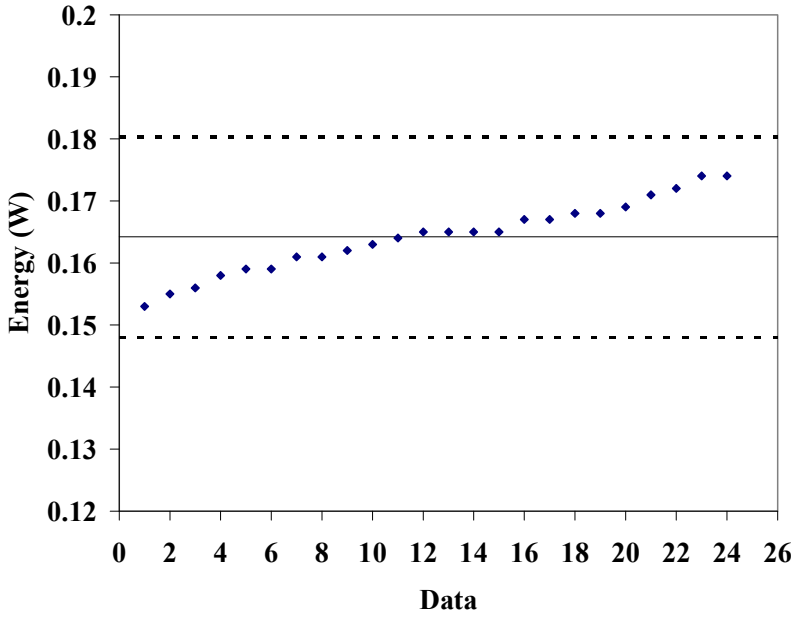

Figure B.10. Plot of the 3rd generation LED array calorimetry experiment investigating the 8 LED constant current driver. Dashed lines represent where outliers would be present according to the Grubbs test.

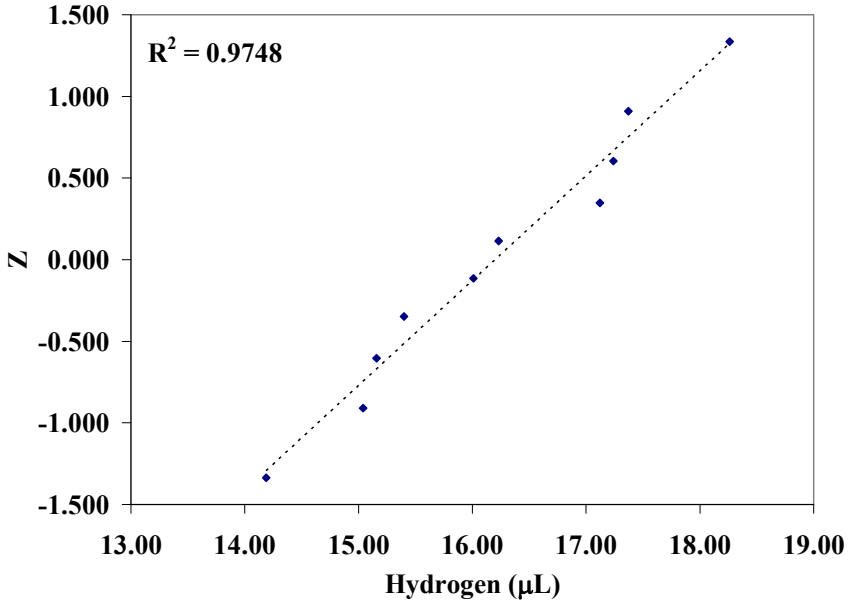

Figure B.11. Rankit plot for photochemical hydrogen production data using the 3rd generation LED array. Data appear to be normally distributed

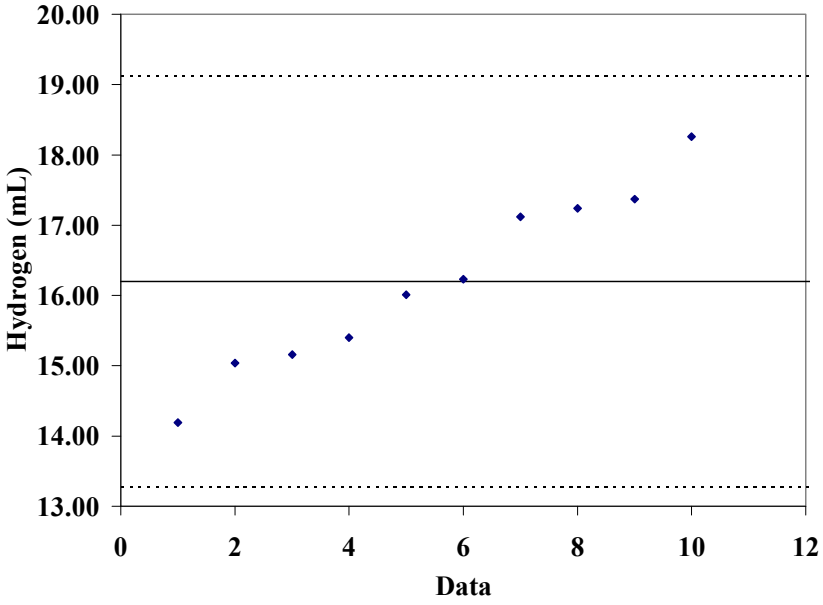

Figure B.12. Plot of photochemical hydrogen production 3rd generation LED array. Dashed lines represent where outliers would be present according to the Grubbs test.